

Modeling moving boundary value problems in electrochemical machining

Tim van der Velden*, Stephan Ritzert, Stefanie Reese, Johanna Waimann

*Institute of Applied Mechanics, RWTH Aachen University, Mies-van-der-Rohe-Str. 1,
D-52074 Aachen, Germany*

Abstract. This work presents a new approach to efficiently model the cathode in the moving boundary value problem of electrochemical machining. Until recently, the process simulation with finite elements had the drawback of remeshing required by the changing surface geometries. This disadvantage was overcome by a novel model formulation for the anodic dissolution that utilizes effective material parameters as well as the dissolution level as an internal variable and, thereby, does not require remeshing. Now, we extend this concept to model arbitrarily shaped and moving cathodes. Two methodologies are investigated to describe the time varying position of the cathode. In the first approach, we change the electric conductivity of elements within the cathode and, in a second approach, we apply Dirichlet boundary conditions on the nodes of corresponding elements. For both methods, elements on the cathode's surface are treated with effective material parameters. This procedure allows for the efficient simulation of industrially relevant, complex geometries without mesh adaptation. The model's performance is validated by means of analytical, numerical and experimental results from the literature. The short computation times make the approach interesting for industrial applications.

Keywords: Electrochemical machining, Finite element method, Moving boundary value problem

1 Introduction

The industry's ever increasing need for the production of complex structures that consist of high strength materials propels the use of electrochemical machining (ECM) (Klocke et al. [2014]). A decisive advantage of the process is the possibility to machine solid materials with exceptional hardness at high removal rates. Moreover, being a contactless process, ECM does not lead to tool wear and does not afflict any mechanical damage to the rim zone of the workpiece. The process utilizes the effect of electrolysis to machine the workpiece by material dissolution

*Corresponding author:
email: tim.van.der.velden@ifam.rwth-aachen.de

Table 1: Relevant symbols

Symbol	Unit	Definition
ϵ_0	[A s/(V m)]	Electric constant
ϵ_r	[-]	Relative permittivity
λ_{cat}	[-]	Cathode ratio
ν_{dis}	[m ³ /(A s)]	Effectively dissolved volume
ρ_E	[A s/m ³]	Electric volume charge density
\mathcal{A}	[-]	Activation function
d	[-]	Dissolution level
\mathbf{D}	[A s/m ²]	Electric displacement field
\mathbf{E}	[V/m]	Electric field strength
I	[A]	Electric current
\mathbf{j}	[A/m ²]	Electric current density
k_E	[A/(V m)]	Electric conductivity
\mathbf{n}	[-]	Normal vector
Q	[A s]	Electric charge
R	[V/A]	Electric resistance
t	[s]	Machining time
v	[V]	Electric potential
V_{cat}	[m ³]	Cathode volume
V_{dis}	[m ³]	Dissolved volume
V_{el}	[m ³]	Element volume
V_{ref}	[m ³]	Reference volume
\mathbf{x}	[m]	Position
$(\bullet)^{\text{CAT}}$		Cathode quantity
$(\bullet)^{\text{EL}}$		Electrolyte quantity
$(\bullet)^{\text{ME}}$		Metal quantity

(DeBarr and Oliver [1968], McGeough [1974], Klocke and König [2007]).

Fig. 1 shows a schematic sketch for an arbitrarily shaped tool. A direct current is applied at the electrodes and yields an electric current at the workpiece's surface that causes the anodic dissolution.

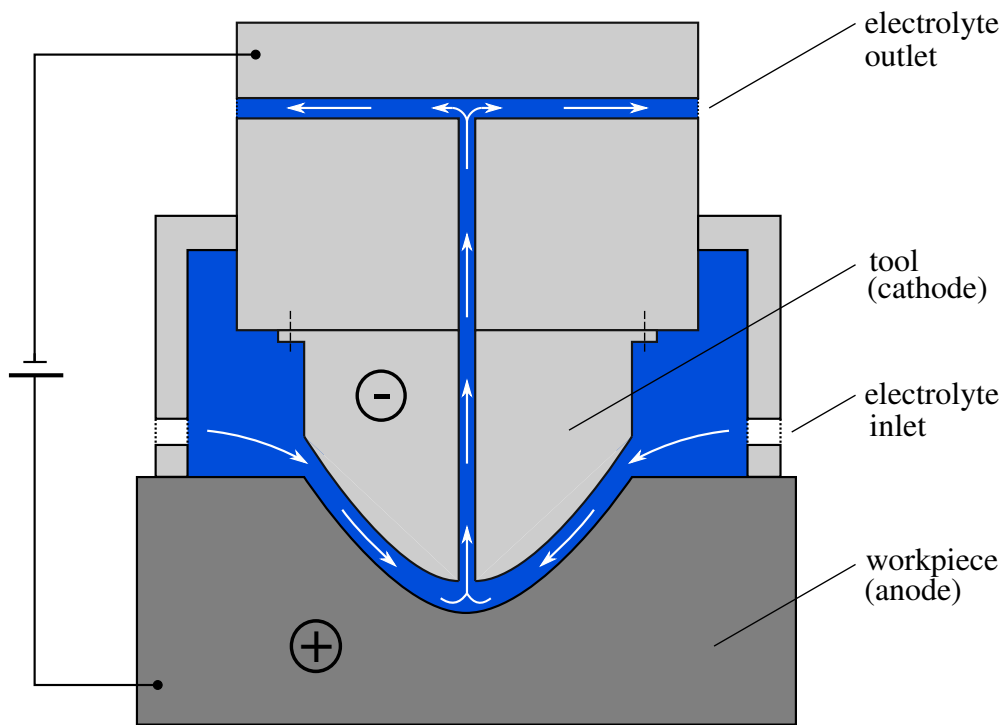


Figure 1: Illustration of the electrochemical machining process (after Klocke and König [2007]).

The fields of application for ECM range from the blade production in turbomachinery manufacturing over the creation of shape optimized cooling bores for improved stress distributions to the precision machining of filigree structures (Klocke and König [2007], Rajurkar et al. [2013]). This wide range of applications motivates the development of efficient simulation methods. Since it is difficult to predict the final shape of the workpiece in ECM, simulations can help to reduce costly trial and error experiments and also to speed up the design process (Hinduja and Kunieda [2013]).

Over time, different numerical methodologies were employed to model ECM: These are the finite difference method (e.g. Tipton [1964], Koenig and Huembs [1977], Kozak [1998]), the boundary element method (e.g. Christiansen and Rasmussen [1976], Hansen in Fasano and Primicerio [1983], Deconinck et al. [1985], Narayanan et al. [1986]) and also the finite element method (FEM) (e.g. Alkire et al. [1978], Jain and Pándey [1980], Hardisty et al. [1993]) that is also employed in this work. According to Hinduja and Kunieda [2013], the FEM possesses the drawback of computationally expensive remeshing due to the changing geometries. To

circumvent remeshing, e.g. Brookes [1984] tried to delete and modify elements close to the anode's surface, which also proved to be expensive. An elegant procedure to adapt the mesh for moving interfaces was presented by Deconinck et al. [2011], who employ an elastic body analogy (Wuilbaut [2008]) to realign the refined region of the mesh with the anodic surface.

However, even state of the art formulations like e.g. the one of Klocke et al. [2018] that models precise ECM with pulsed current and oscillating cathode still need remeshing to model the anodic dissolution and the cathode movement by assigning separate domains for fluid and solid. To our best knowledge, previous models lack a continuous formulation of the dissolution process without the requirement of mesh adaption.

Therefore, we proposed a novel approach that works entirely without remeshing and models the anodic dissolution in ECM with effective material parameters and an internal variable (van der Velden et al. [2021]). In this work, the novel approach based on effective material parameters serves to model the movement of arbitrarily shaped cathodes in ECM. Previous studies were restricted to a stationary cathode or a simplified modeling of the cathode feed. The aspiration to investigate industrially relevant and complex problems underlines the necessity of this contribution to efficiently and accurately model the cathode.

To this end, this work investigates two approaches for modeling the cathode. In method A, the electric conductivity of the elements within the cathode is modified. In method B, Dirichlet boundary conditions are applied on all nodes within the cathode. Both methodologies are based on effective material parameters for elements on the cathode's surface and, thereby, allow for a simulation entirely without remeshing.

Nowadays, following the earlier works of e.g. Antonova and Looman [2005], Pérez-Aparicio et al. [2007], numerous authors investigate electrically coupled multifield problems. Hofmann et al. [2020] conduct e.g. electro-chemo-mechanical simulations, Wu and Li [2018] additionally include thermal and Liu et al. [2020] magnetic effects to name only a few. We, however, focus in this work on the modeling of the moving boundary value problem and, therefore, for simplicity, restrict ourselves to the electric field problem, since the electric current density is the driving force in electrochemical machining. The thermal field is thus assumed to be constant.

Moreover, the model's efficiency could further be improved by advanced finite element technology using reduced integration and hourglass stabilization, which has already been applied successfully to different multifield problems, e.g. for electromagnetic (Reese et al. [2005]) and thermomechanical coupling (Juhre and Reese [2010]) as well as gradient-extended damage (Barfusz et al. [2021, 2022]). Additionally, the incorporation of initially and induced anisotropic material behavior following e.g. Holthusen et al. [2020] and Reese et al. [2021] promises an interesting model extension in future works.

Outline of the work. In Section 2, the electric balance equation and the constitutive laws

are introduced. Thereafter, we give a brief summary of the dissolution model in Section 3 and comment on numerical aspects in Section 4. In Section 5, we present the new methodologies for modeling the cathode. In Section 6.1, analytical reference solutions serve to validate the model's accuracy and additional studies regarding the runtime and the choice of the effective material parameters are conducted. In Sections 6.2 and 6.3, challenging examples with numerical and experimental references are investigated. In Section 6.4, the model's ability to model complex cathode shapes by simulating a blade machining process is confirmed. A conclusion is provided in Section 7.

Notational conventions. In this work, italic characters a , A denote scalars and zeroth-order tensors and bold-face italic characters \mathbf{b} , \mathbf{B} refer to vectors and first-order tensors. The operators $\text{div}(\bullet)$ and $\text{grad}(\bullet)$ denote the divergence and gradient operation of a quantity with respect to Cartesian coordinates. A dot \cdot defines the single contraction of two tensors. The time derivative of a quantity is given by $(\dot{\bullet})$. A tilde $(\tilde{\bullet})$ defines a prescribed quantity on the corresponding boundary. Moreover, Table 1 lists the relevant symbols and states, if applicable, the corresponding SI units.

2 Constitutive modeling

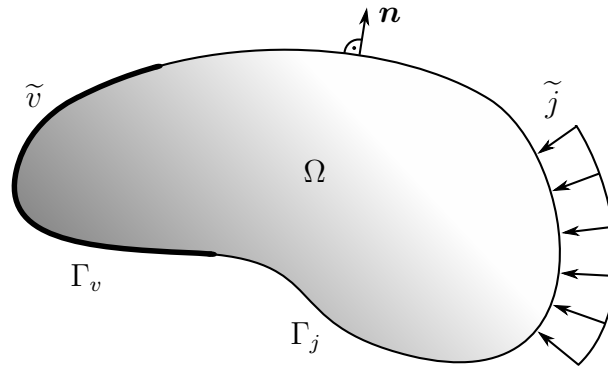


Figure 2: Illustration of the electric boundary value problem.

The present contribution focuses on the modeling of moving cathode geometries. As mentioned in Section 1, we consider isothermal problems and, therefore, solely present the balance of electric charge including Dirichlet and Neumann boundary conditions (see Fig. 2 and cf. Jackson [1962]):

$$\begin{aligned}
 \dot{\rho}_E + \text{div}(\mathbf{j}) &= 0 && \text{in } \Omega \\
 v &= \tilde{v}(t) && \text{on } \Gamma_v \\
 \mathbf{j} \cdot \mathbf{n} &= \tilde{j} && \text{on } \Gamma_j
 \end{aligned} \tag{1}$$

The primary variable of this problem is the electric potential v . The movement of the cathode's surface is incorporated by considering time varying Dirichlet boundary conditions $\tilde{v}(t)$ for the electric potential. The electric field strength \mathbf{E} , the electric displacement field \mathbf{D} and the electric volume charge density ρ_E read

$$\mathbf{E} = -\text{grad}(v), \quad \mathbf{D} = \epsilon_0 \epsilon_r \mathbf{E}, \quad \rho_E = \text{div}(\mathbf{D}) \quad (2)$$

where ϵ_0 denotes the electric constant and ϵ_r the relative permittivity. The constitutive law of the electric current density \mathbf{j} yields

$$\mathbf{j} = k_E \mathbf{E} + \epsilon_0 \epsilon_r \dot{\mathbf{E}} \quad (3)$$

where k_E denotes the electric conductivity and $\dot{\mathbf{E}}$ the time derivative of the electric field strength \mathbf{E} . Finally, the weak form g_v may be obtained as

$$g_v := - \int_{\Omega} \left(k_E \mathbf{E} + 2 \epsilon_0 \epsilon_r \dot{\mathbf{E}} \right) \cdot \text{grad}(\delta v) \, dV + g_{\bar{j}} = 0 \quad (4)$$

where δv is an arbitrary test function and $g_{\bar{j}}$ a prescribed electric current density.

For the linearization of the problem and the additional consideration of electro-thermal coupling, the reader is kindly referred to van der Velden et al. [2021].

3 Anodic dissolution

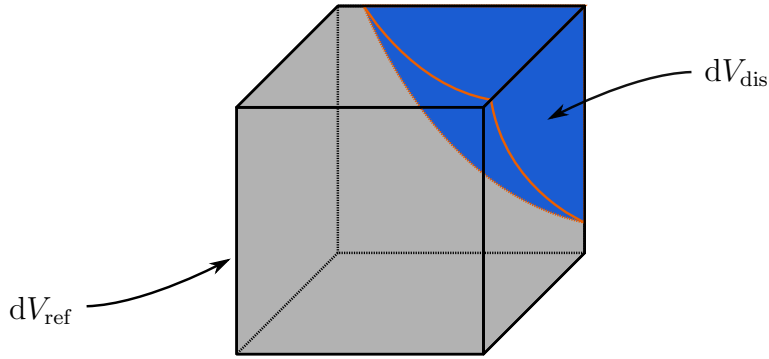


Figure 3: Visualization of the reference volume dV_{ref} and the incremental dissolved volume dV_{dis} . The orange line surrounds the anode's surface.

This work utilizes the model of van der Velden et al. [2021] to describe the anodic dissolution. Analogously to damage modeling (e.g. Kachanov [1958]), an internal variable in combination with effective material parameters serves to describe the transition from an undissolved material state to a fully dissolved one. In the first situation, there is only metal present. In the second situation, the metallic material has been fully dissolved such that only electrolyte remains. The

dissolution level $d \in [0, 1]$ states the ratio $d = dV_{\text{dis}}/dV_{\text{ref}}$ of the incremental dissolved volume dV_{dis} to the volume of the corresponding reference volume dV_{ref} (see Fig. 3). Hence, the rate of the dissolution level yields the relation

$$\dot{d} dV_{\text{ref}} = d\dot{V}_{\text{dis}} \quad (5)$$

where it is assumed that dV_{ref} is constant over time. In the formulation, we employ a modified version of Faraday's law of electrolysis to correlate the dissolved volume with the passing electric charges (Klocke and König [2007]). Using the material parameter ν_{dis} that represents the dissolved volume per electric charge, and the activation function \mathcal{A} as well as the time derivative of the incremental electric charge $d\dot{Q}$, the time derivative of the incrementally dissolved volume reads

$$d\dot{V}_{\text{dis}} = \nu_{\text{dis}} \mathcal{A} d\dot{Q}. \quad (6)$$

Moreover, we consider the definition of the activation function

$$\mathcal{A}(\mathbf{x}, t) = \begin{cases} 1, & \text{contact metal-electrolyte} \\ 0, & \text{else} \end{cases} \quad (7)$$

that depends on the position \mathbf{x} and time t and indicates whether the material has contact with the electrolyte which is a requirement for the chemical reaction. Further, the connection between the time derivative of the incremental electric charge $d\dot{Q}$ and the incremental electric current dI is given as

$$d\dot{Q} = dI, \quad (8)$$

where $dI(\mathbf{j}, d)$ depends on the electric current density \mathbf{j} and the dissolution level d . With Eq. (8), we accordingly rewrite Eq. (5) to

$$\dot{d} dV_{\text{ref}} = \nu_{\text{dis}} \mathcal{A}(\mathbf{x}, t) dI(\mathbf{j}, d). \quad (9)$$

Finally, we define the effective material parameters. Previously, the volume average of metal and electrolyte properties (Fig. 4a) was considered to read

$$(\bar{\bullet})^{\text{P}} = (1 - d) (\bullet)^{\text{ME}} + d (\bullet)^{\text{EL}}. \quad (10)$$

This constitutes a parallel connection for the rule of mixture. Motivated by the analogy of electrical circuits (Fig. 4), this work additionally considers a series connection (Fig. 4b) for the rule of mixture between metal and electrolyte:

$$(\bar{\bullet})^{\text{S}} = [(1 - d) / (\bullet)^{\text{ME}} + d / (\bullet)^{\text{EL}}]^{-1} \quad (11)$$

In Section 6.1, the influence of the rule of mixture on the dissolved volume is studied.

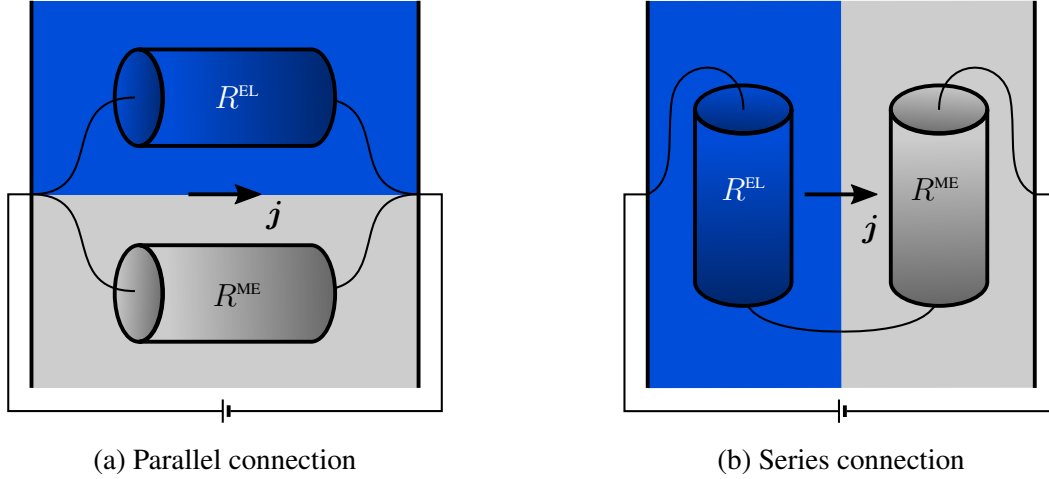


Figure 4: Parallel (a) and series connection (b): Depending on the rule of mixture, different electrical circuits for a horizontal electric current density j passing between the electrodes through the electrical resistances R^{ME} and R^{EL} are considered.

4 Numerical aspects

For the time and spatial discretization, we employ the backward Euler method and the finite element method, respectively. For detailed information on the latter, the reader is kindly referred to Hughes [1987] and Zienkiewicz et al. [2005]. The specific element residual vectors and stiffness matrices may be found in van der Velden et al. [2021].

The formulation is implemented into the finite element software FEAP (Taylor and Govindjee [2020]). The activation function \mathcal{A} (Eq. (7)) is incorporated into the solution algorithm by an update procedure at the end of every time step. When a finite element dissolves completely, it triggers the update procedure and activates all adjacent metal elements that have a shared surface with the dissolved element. The cut-off volume V_{co} , which was investigated in van der Velden et al. [2021], denotes the theoretically dissolved volume in an integration point that is neglected when $d_{n+1} > 1$ is reset to $d_{n+1} = 1$. In the present formulation, V_{co} is allocated to the activated elements. Thereby, the formulation allows for the use of larger time steps and, hence, reduces computation time.

5 Cathode modeling

The driving force of the electric current is the potential difference Δv which is applied between cathode and anode. The domain of the cathode is characterized by the property $v = 0$. To describe moving cathode geometries with arbitrary shapes, the model has to account for the time varying Dirichlet boundary conditions $\tilde{v}(t)$, i.e. to prescribe a zero electric potential on

the surface and within the tool's geometry. Here, it is particularly advantageous that the new modeling approach does not require any mesh adaptation during the simulation despite the time dependent boundary conditions.

5.1 Method A

Two different methods are employed to model the aforementioned condition. In the first, method A, the electric conductivities of the finite elements within the cathode are modified and the corresponding values are set numerically to infinity (Fig. 5). The electric resistance of these elements is numerically zero and no change of the electric potential can be observed within the cathode. Thus, the equipotential line with $v = 0$ coincides with the cathode's surface as long as the electric potential v is prescribed at one point within the cathode. The advantage of method A is the straightforward implementation, since no modification of the global system of equations is required. This approach is inspired by Hardisty et al. [1993] who assign to each element a different material type depending on its classification as tool, workpiece or electrolyte.

5.2 Method B

In the second, method B, a zero electric potential is applied directly on all nodes within the cathode (Fig. 6). To account for the cathode feed, this approach requires an adaptation and a renumbering of the global system of equations in every time step. However, this procedure is computationally still beneficial, since the number of degrees of freedom reduces for regular cathode geometries steadily throughout the simulation when the number of fixed degrees of freedom inside the cathode increases. Furthermore, method B allows for the investigation of special cathode shapes, e.g. electrochemical wirecutting where the zero electric potential is defined only in the thin wire domain.

5.3 Effective material parameters

Both models follow the conceptual approach of the dissolution model and work for a constant finite element mesh. Naturally, the cathode's surface does not necessarily coincide with the finite elements' edges. Thus, elements exist that are partially electrolyte and partially cathode (see Fig. 7). Analogously to the dissolution level d , we define the cathode ratio

$$\lambda_{\text{cat}} = \frac{V_{\text{cat}}}{V_{\text{el}}} \quad (12)$$

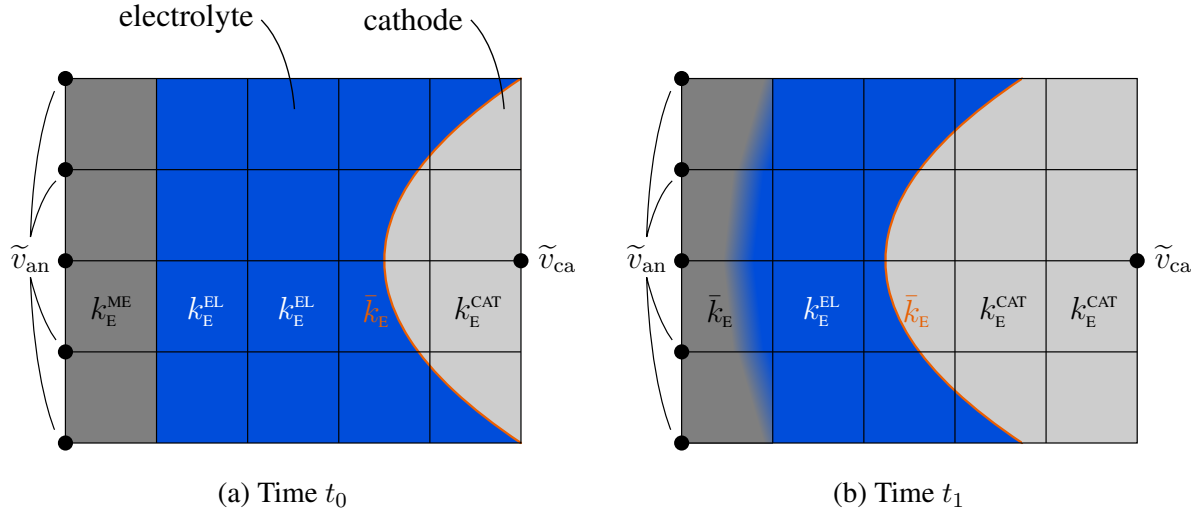


Figure 5: Illustration of method A. The cathode moves towards the anode from time t_0 to time t_1 . The electric potential v is fixed at one node within the cathode and the cathode feed is modeled by assigning each element within the cathode an infinite electric conductivity k_E^{CAT} . Exemplarily, the electric conductivity in a horizontal line of elements is shown at t_0 and t_1 and a black dot denotes a fixed degree of freedom.

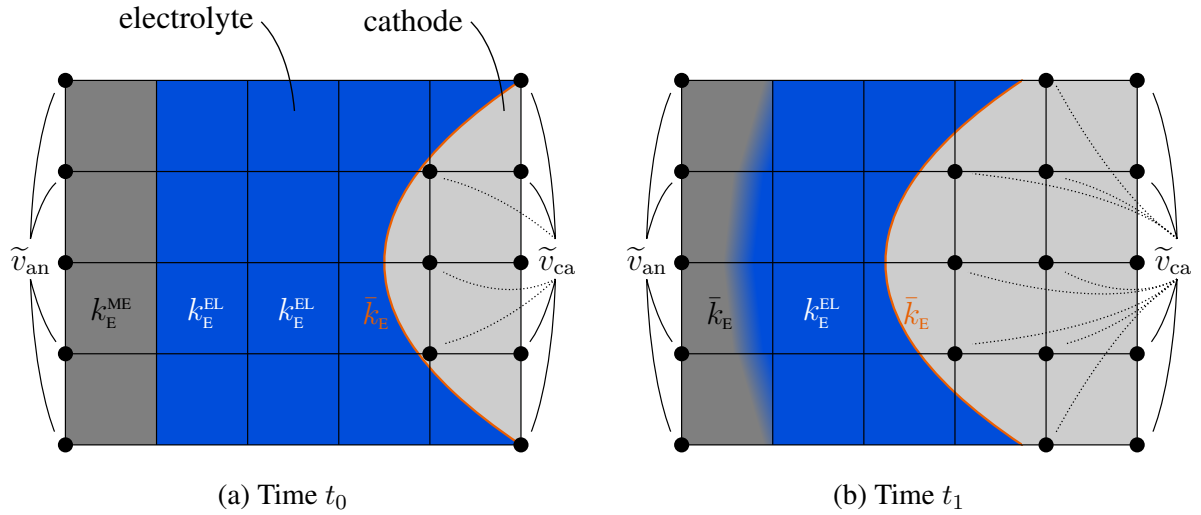


Figure 6: Illustration of method B. The cathode moves towards the anode from time t_0 to time t_1 . The electric potential v is fixed at all nodes within the cathode and the cathode feed is modeled by assigning additional Dirichlet boundary conditions. A black dot denotes a fixed degree of freedom.

that states the volume of the cathode in a finite element V_{cat} compared to the total volume of this element V_{el} . The polyeder's volume V_{cat} is computed via tetrahedralization using a Delaunay triangulation algorithm developed by Joe [1991]. Moreover, following the definition of Eqs. (10) and (11), we define the effective material parameters of partial cathode elements for a parallel connection as

$$(\bar{\bullet})^{\text{P}} = (1 - \lambda_{\text{cat}}) (\bullet)^{\text{EL}} + \lambda_{\text{cat}} (\bullet)^{\text{CAT}} \quad (13)$$

and for a series connection respectively as

$$(\bar{\bullet})^{\text{S}} = [(1 - \lambda_{\text{cat}}) / (\bullet)^{\text{EL}} + \lambda_{\text{cat}} / (\bullet)^{\text{CAT}}]^{-1} \quad (14)$$

where $(\bullet)^{\text{EL}}$ again denotes the material parameters of the electrolyte and $(\bullet)^{\text{CAT}}$ those of the cathode.

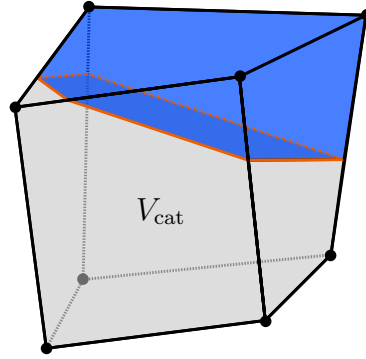


Figure 7: A finite element that is partially cathode and partially electrolyte. V_{cat} defines the finite element's volume inside the cathode and the orange line surrounds the cathode's surface.

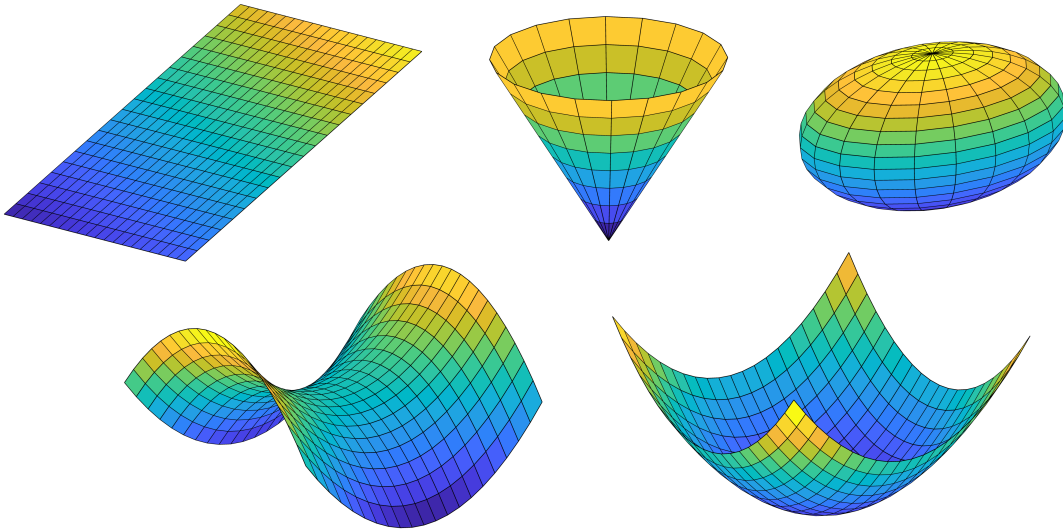


Figure 8: Basic geometries used for the cathode assembly: Plane, cone, ellipsoid and paraboloids.

The mathematical description of the cathode geometry follows set theory. Fig. 8 shows different basic geometries that can be combined by conjunction in subsets. These subsets are combined by disjunction to obtain the total cathode geometry (see Fig. 9). This two step procedure is necessary to fulfill the distributive property of disjunctions over conjunctions. The position vector which is inherent in each geometry models the cathode feed by incrementally updating its coordinates in every time step. The implementation features also additional options like the rotation of a geometry or the consideration of either the enclosed volume of a geometry or the volume outside of a geometry.

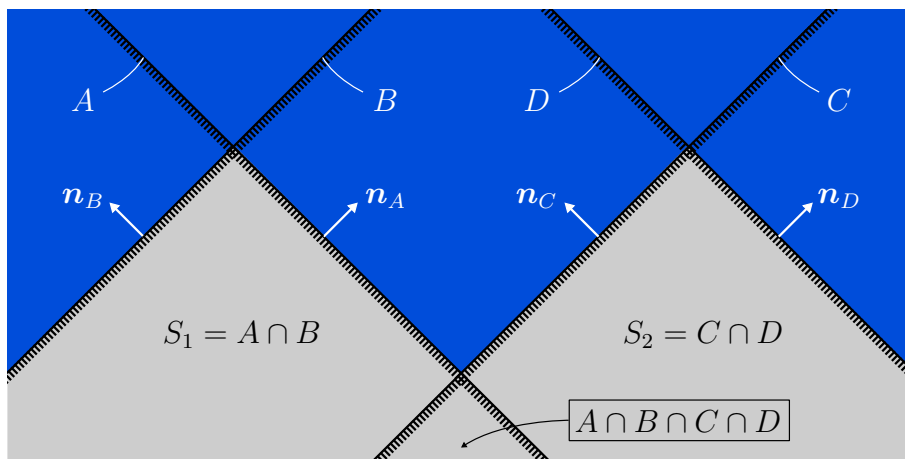


Figure 9: Illustration of a cathode assembly by conjunction (intersection) and disjunction (union). The subsets S_1 and S_2 are obtained by the conjunction of set A and B and set C and D , respectively. The disjunction of all subsets ($S_1 \cup S_2$) yields the total cathode geometry. A conjunction of set A , B , C and D without the definition of subsets would yield a different cathode geometry ($A \cap B \cap C \cap D \neq S_1 \cup S_2$).

In a previous work, the theorem of intersecting lines served to model the cathode feed by a simplified approach. However, this procedure was restricted to processes with planar cathodes where the initial working gap width coincided with the gap width of the dynamic equilibrium state for a given feed rate. The new methodology allows for the investigation of arbitrary processes with varying process parameters as shown in Section 6.

Fig. 10, finally, provides the resulting set of equations for the presented model.

6 Numerical examples

In this section, we employ the previously developed methodology to model the cathode feed in different applications. Furthermore, we compare the runtimes of method A and B. Analytical and experimental reference solutions serve to validate the methodology's performance and accuracy. Finally, we investigate an electrochemical blade manufacturing process.

- Balance equation and boundary conditions

$$\begin{aligned} \rho_E + \operatorname{div}(\mathbf{j}) &= 0 & \text{in } \Omega & & \rho_E &= \operatorname{div}(\mathbf{D}) \\ v &= \tilde{v}(t) & \text{on } \Gamma_v & & \text{with } \mathbf{D} &= \epsilon_0 \bar{\epsilon}_r \mathbf{E} \\ \mathbf{j} \cdot \mathbf{n} &= \tilde{j} & \text{on } \Gamma_j & & \mathbf{E} &= -\operatorname{grad}(v) \end{aligned}$$
- Constitutive law

$$\mathbf{j} = \bar{k}_E \mathbf{E} + \epsilon_0 \bar{\epsilon}_r \dot{\mathbf{E}}$$
- Effective material parameters anode

$$\begin{aligned} (\bar{\bullet})^P &= (1 - d) (\bullet)^{\text{ME}} + d (\bullet)^{\text{EL}} \\ (\bar{\bullet})^S &= [(1 - d) / (\bullet)^{\text{ME}} + d / (\bullet)^{\text{EL}}]^{-1} \end{aligned}$$
- Effective material parameters cathode

$$\begin{aligned} (\bar{\bullet})^P &= (1 - \lambda_{\text{cat}}) (\bullet)^{\text{EL}} + \lambda_{\text{cat}} (\bullet)^{\text{CAT}} \\ (\bar{\bullet})^S &= [(1 - \lambda_{\text{cat}}) / (\bullet)^{\text{EL}} + \lambda_{\text{cat}} / (\bullet)^{\text{CAT}}]^{-1} \end{aligned}$$

Figure 10: Resulting set of equations for the moving boundary value problem.

The material parameters employed in the simulations stem from Table 2, if not explicitly stated otherwise. For simplicity, we consider only isothermal problems with a constant temperature of 50 K.

Table 2: Material parameters and physical constants

Symbol	Unit	Value
k_E^{CAT}	[A/(V m)]	1.000×10^{12}
k_E^{EL}	[A/(V m)]	1.600×10^1
k_E^{ME}	[A/(V m)]	4.625×10^6
ϵ_r^{CAT}	[-]	1.000×10^0
ϵ_r^{EL}	[-]	8.000×10^1
ϵ_r^{ME}	[-]	1.000×10^0
ϵ_0	[A s/(V m)]	8.854×10^{-12}
ν_{dis}	[m ³ /(A s)]	1.000×10^{-11}

6.1 Planar cathode - analytical validation

In the first example, we discuss a planar cathode (see Fig. 11) with an analytical reference solution analogously to van der Velden et al. [2021]. The dimensions read $l = h = 1$ mm with

a thickness of 0.1 mm and a constant feed rate of $\dot{x}_{ca} = 0.01\text{mm/s}$ is employed with a potential difference of $\Delta v = 20\text{ V}$.

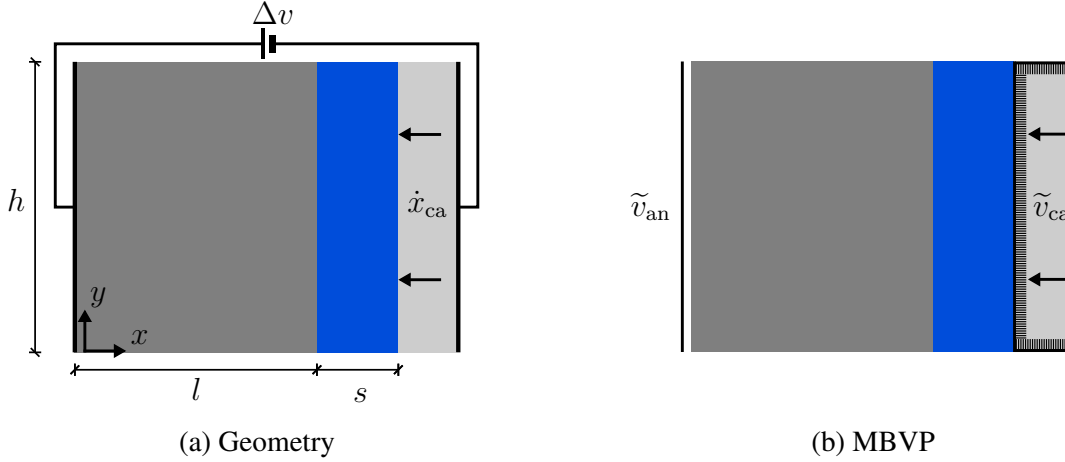


Figure 11: Geometry and moving boundary value problem for a planar cathode.

At the beginning, we utilize an initial working gap width of $s_{\text{init}} = 0.32\text{ mm}$ that equals the gap width of the dissolution process in the dynamic equilibrium state (cf. Klocke and König [2007]). Fig. 12 shows the comparison of the parallel (Eqs. (10) and (13)) the series connection (Eqs. (11) and (14)). The dissolved volume of the finite element simulation after 60 s, which is normalized with respect to the analytical solution, is given for different time increments and element densities. Structured meshes are employed.

Although the results of the parallel connection converge against the analytical solution for fine meshes, they still show an error of +1.8 % for the finest discretization. The electric resistance of a dissolving element is underestimated by the parallel connection in this application, since the electric charges do not necessarily pass the electrolyte resistance in these elements (cf. Fig. 4). Thereby, the electric current and the dissolved volume are overestimated by the model. The series connection, however, yields the correct solution regardless of the time step size and element density. Moreover, method A and B yield identical results.

Next, the runtime of method A and B are compared in Fig. 13. The coarser meshes, which have fewer degrees of freedom compared to the fine meshes, yield similar runtimes for both methods. Nevertheless for the finest mesh, method B is 16.3 % faster, since the reduction of the size of the global system of equations yields a significant impact on the computational efficiency. Afterwards, we investigate this example using vertically and horizontally distorted meshes which stem from van der Velden et al. [2021]. Fig. 14 shows the results for the series connection and method B with $\Delta t = 10^{-3}\text{ s}$. For the most severe distortions, the dissolved volume is underestimated in the simulation (mesh 10 \downarrow 80: -6.5 %, mesh 80 \rightarrow 10: -9.3 %). However, the results improve for moderate distortions (mesh 20 \downarrow 80: -5.1 %, mesh 80 \rightarrow 20: -3.9 %) and converge towards the analytical solution for minor distortions (mesh 40 \downarrow 80:

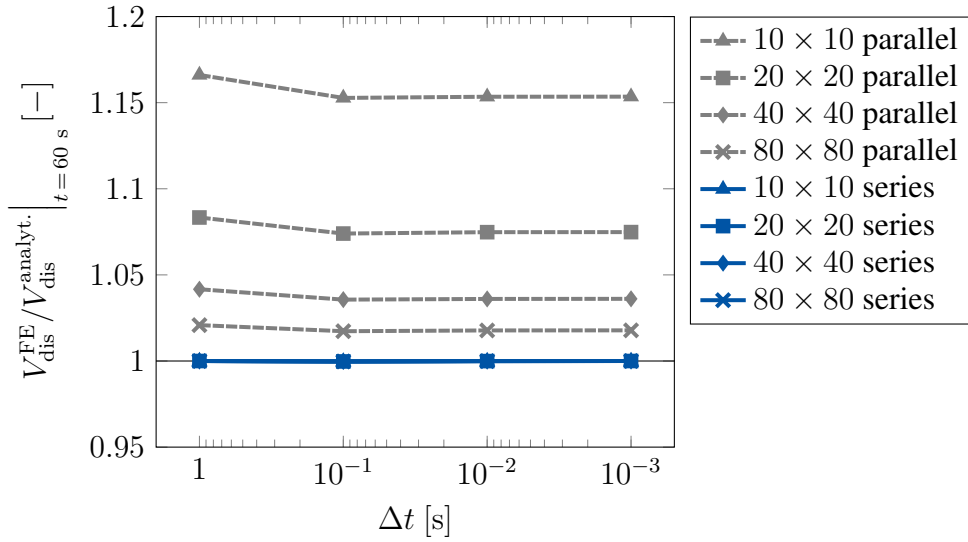


Figure 12: Comparison of the dissolved volume at $t = 60$ s of the finite element simulation and the analytical solution for the parallel and series connection with structured meshes for different element densities per mm^2 . The simulations with method A and B yield the same results.

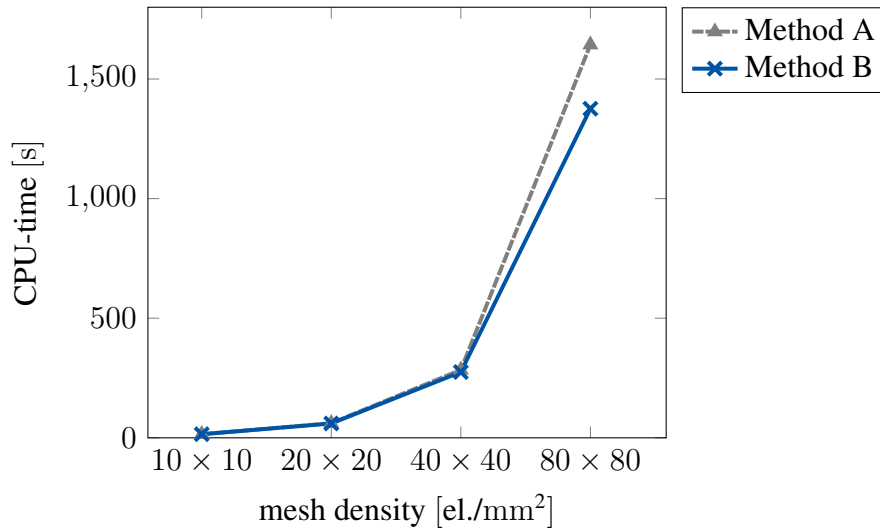


Figure 13: Comparison of the runtime of method A and B. Structured meshes are employed with the series connection and a time increment of $\Delta t = 10^{-1}$ s.

−0.8 %, mesh 80 → 40: −1.2 %).

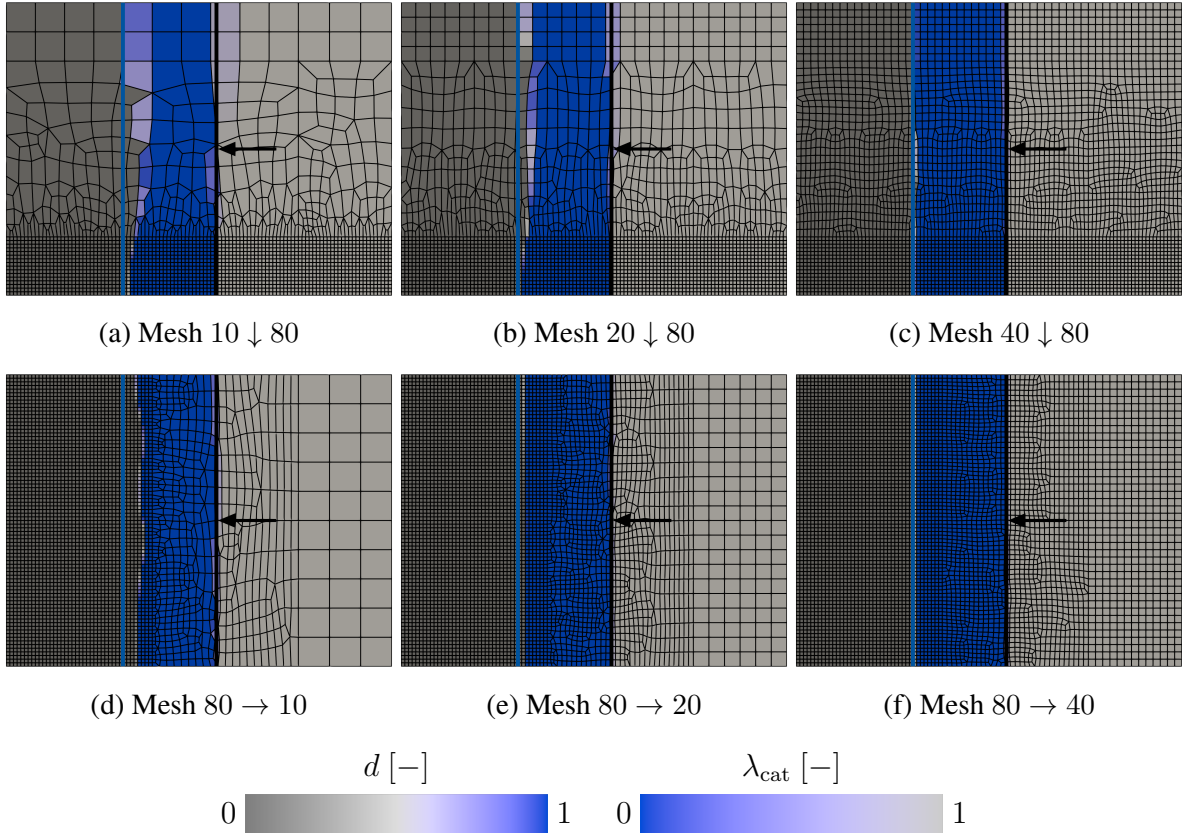


Figure 14: The dissolution level d and the cathode ratio λ_{cat} for distorted meshes at $t = 60$ s. The time increment reads $\Delta t = 10^{-3}$ s and the series connection as well as method B are employed. The vertical blue line provides the anode’s surface according to the analytical reference solution. The vertical black line indicates the cathode surface’s position and the black arrow gives the direction of the cathode feed.

Figs. 15 and 16 show the comparison of the parallel and series connection for different time step sizes. Both rules of mixture yield for all meshes already with the second largest time increment a stable solution that changes only marginally with a further reduction of the time increment. The parallel connection yields for the fine meshes with $\Delta t = 1$ s a solution close to the analytical result. However, this is not the model’s final outcome, since convergence with respect to the time step size is not yet obtained. In the end, the dissolved volume is overestimated by the parallel connection for the different configurations and it yields also for minor distortions still an error of +4.5 % (mesh 40 ↓ 80) and +4.2 % (mesh 40 → 80). Based on these results, the remaining examples utilize the series connection as rule of mixture.

To demonstrate the flexibility of the new approach, Fig. 17 shows the evolution of the working gap width s during the machining process with a constant feed rate $\dot{x}_{\text{ca}} = 0.015$ mm/s and varying initial widths s_{init} . All graphs concur at the analytical solution of $s = 0.213$ mm and

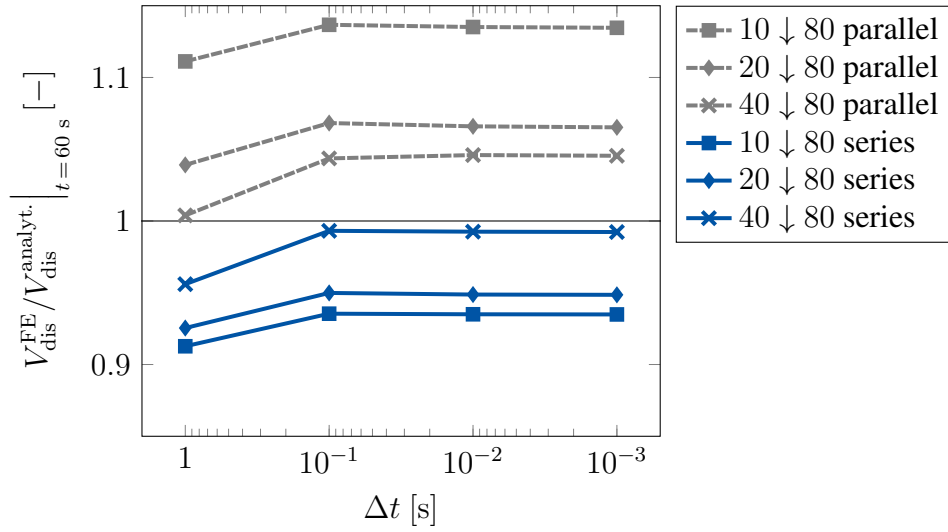


Figure 15: Comparison of the dissolved volume at $t = 60$ s of the finite element simulation using method B and the analytical solution for the parallel and series connection with vertically distorted meshes.

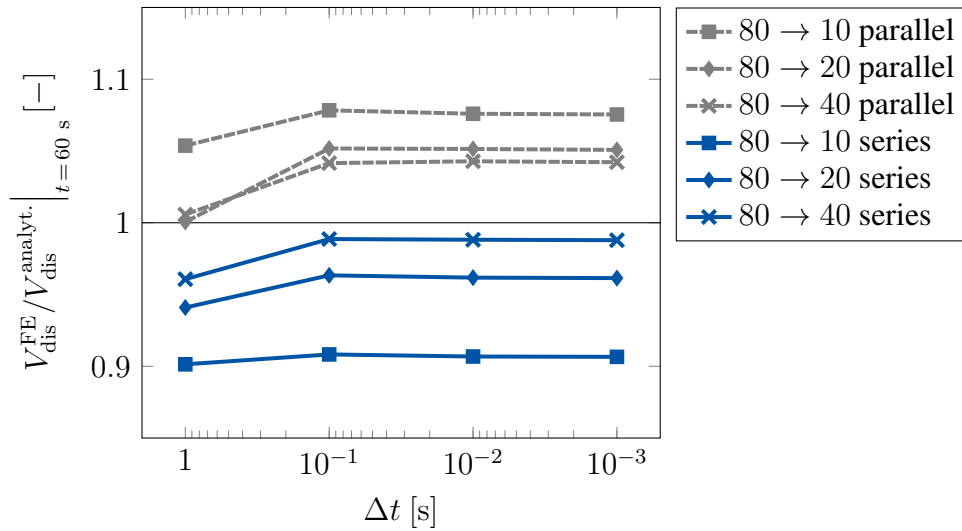


Figure 16: Comparison of the dissolved volume at $t = 60$ s of the finite element simulation using method B and the analytical solution for the parallel and series connection with horizontally distorted meshes.

confirm the correct operation of the method, since the convergence of the gap widths requires the exact modeling of the cathode.

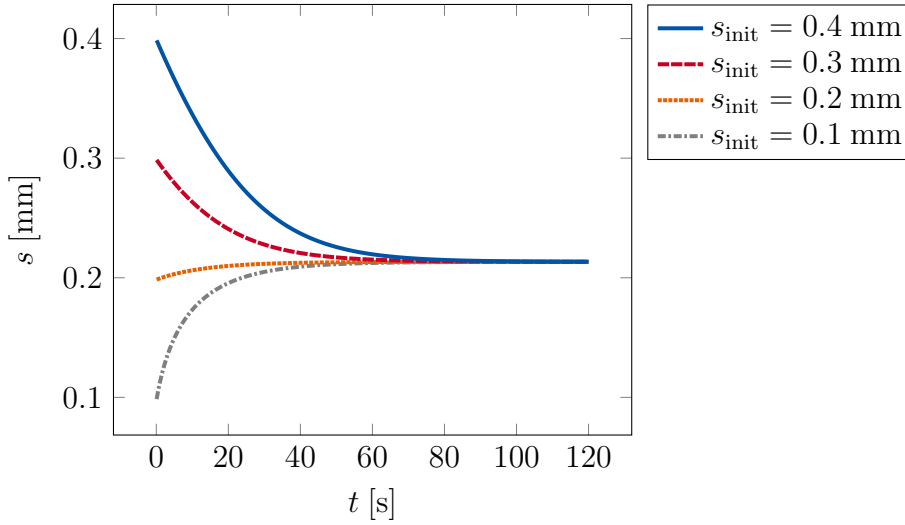


Figure 17: Investigation of the evolution of the working gap width s for different initial widths s_{init} . The feed rate is constant at $\dot{x}_{\text{ca}} = 0.015$ mm/s, $\Delta t = 0.1$ s and method B is employed.

Furthermore, Fig. 18 shows the evolution of the gap width s for the same initial value s_{init} but different feed rates \dot{x}_{ca} . For a higher feed rate, the gap width decreases (cf. Klocke and König [2007]) until it reaches the dynamic equilibrium state ($\dot{x}_{\text{ca}} = 0.010 - 0.020$ mm/s). For a lower feed rate, the working gap widens ($\dot{x}_{\text{ca}} = 0.005$ mm/s). This study again confirms the versatility of the new framework.

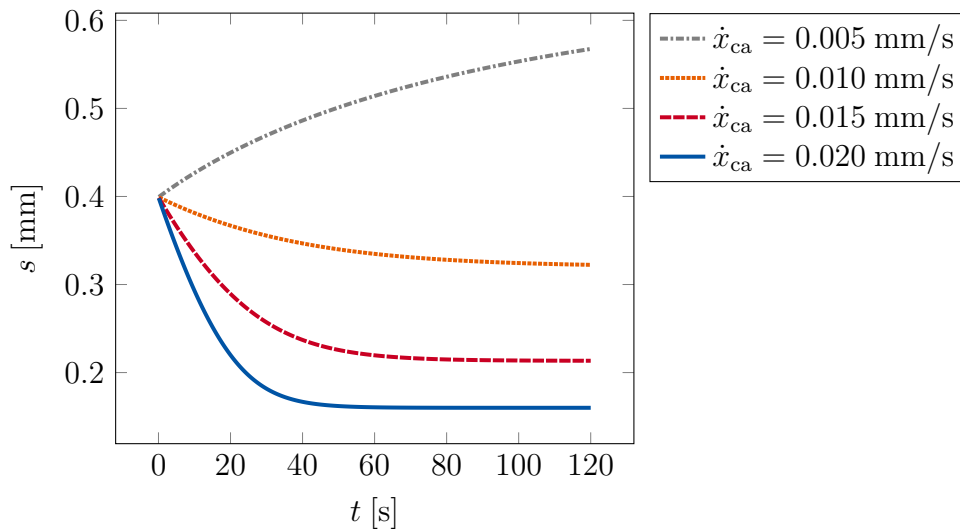


Figure 18: Investigation of the evolution of the working gap width s for different feed rates \dot{x}_{ca} . The initial width is $s_{\text{init}} = 0.4$ mm, $\Delta t = 0.1$ s and method B is employed.

6.2 Parabolic cathode - Hardisty and Mileham [1999]

In the second example, we consider a parabolically shaped cathode (Fig. 19) which has formerly been studied by Hardisty and Mileham [1999]. The material parameters read $k_E^{\text{ME}} = 6.670 \times 10^6 \text{ A}/(\text{V m})$, $k_E^{\text{EL}} = 15 \text{ A}/(\text{V m})$ and $\nu_{\text{dis}} = 3.696 \times 10^{-11} \text{ m}^3/(\text{A s})$. The cathode moves with a constant feed rate $\dot{x}_{\text{ca}} = 0.0145 \text{ mm/s}$ towards the anode with $\Delta t = 0.34483 \text{ s}$ yielding a displacement of 0.005 mm per time step and a total displacement of 2.5 mm after 500 time steps. The geometric dimensions are $l = 2 \text{ mm}$, $h_1 = 3 \text{ mm}$, $h_2 = 1.5 \text{ mm}$, $s = 0.5 \text{ mm}$ with a thickness of 0.5 mm. The parabola is defined by the function $f(x) = 0.375x^2 + 3.5$ and the potential difference is $\Delta v = 10 \text{ V}$. Due to symmetry, only the left part $x \in [-2, 0]$ is simulated. We use structured meshes with finite element (el.) discretizations from $5 \times 5 \text{ el./mm}^2$ to $40 \times 40 \text{ el./mm}^2$.

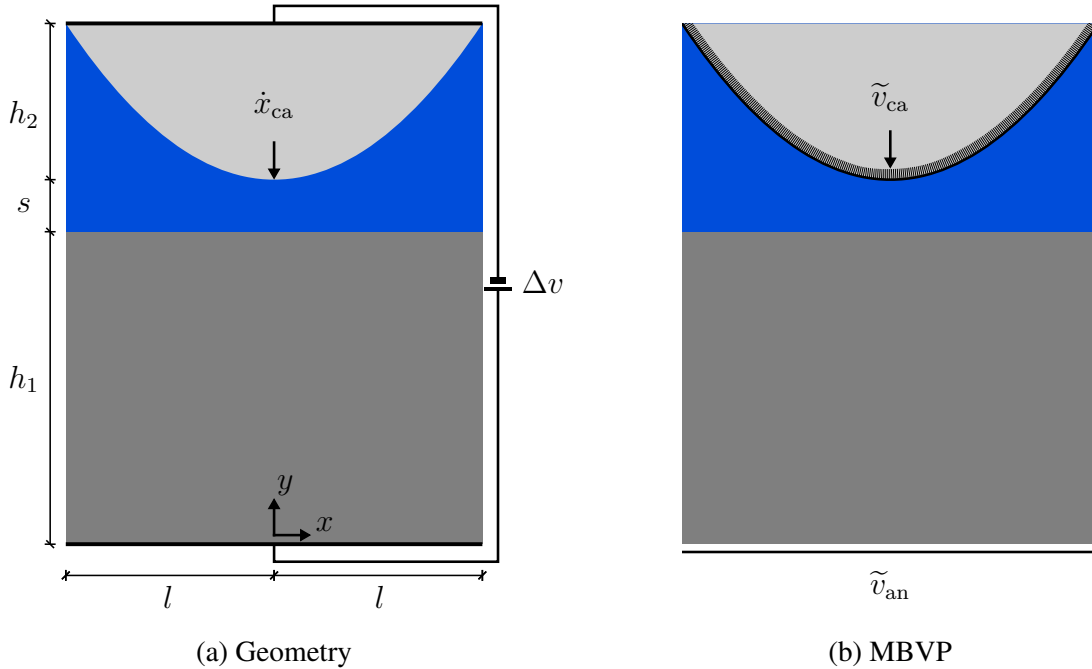


Figure 19: Geometry and moving boundary value problem for a parabolic cathode (cf. Hardisty and Mileham [1999]).

Fig. 20 shows the dissolved volume over time for the different mesh densities normalized to the solution of the finest mesh with $V_{\text{dis}}^{\text{ref.}} = 0.775 \text{ mm}^3$. The curves agree well and mesh convergence is proven.

In Fig. 21, we compare the shape of the anode at the end of the simulation for different mesh discretizations. With finer discretizations, the surface profile becomes smoother. Nevertheless, already the coarsest discretization allows for an accurate prediction of the final work piece shape. The working gap width at the axis of symmetry at the end of the simulation is $s = 0.345 \text{ mm}$ and agrees with the reference solution of Hardisty and Mileham [1999] of $s^{\text{ref.}} =$

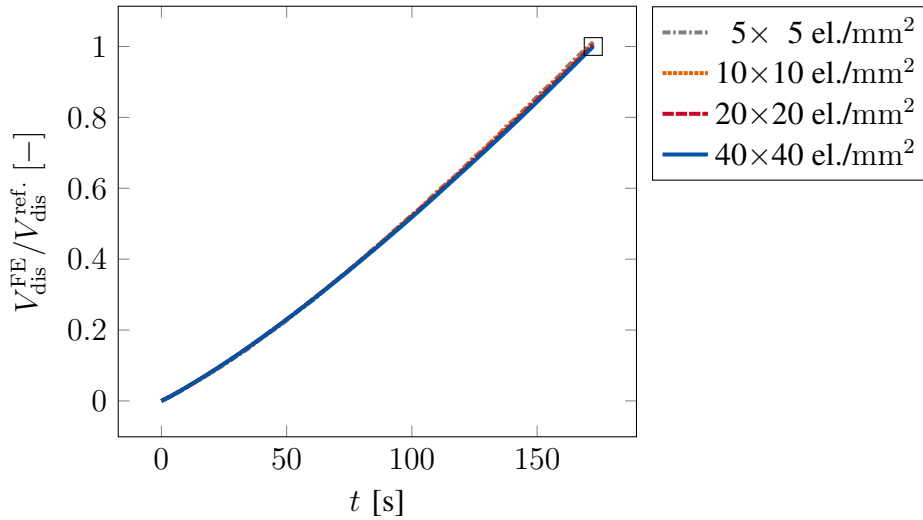


Figure 20: The dissolved volume over time computed with method B for different mesh densities. The graphs are normalized to the solution of the finest mesh with $\Delta t = 0.34483$ s. The black box indicates the point of comparison in Fig. 21.

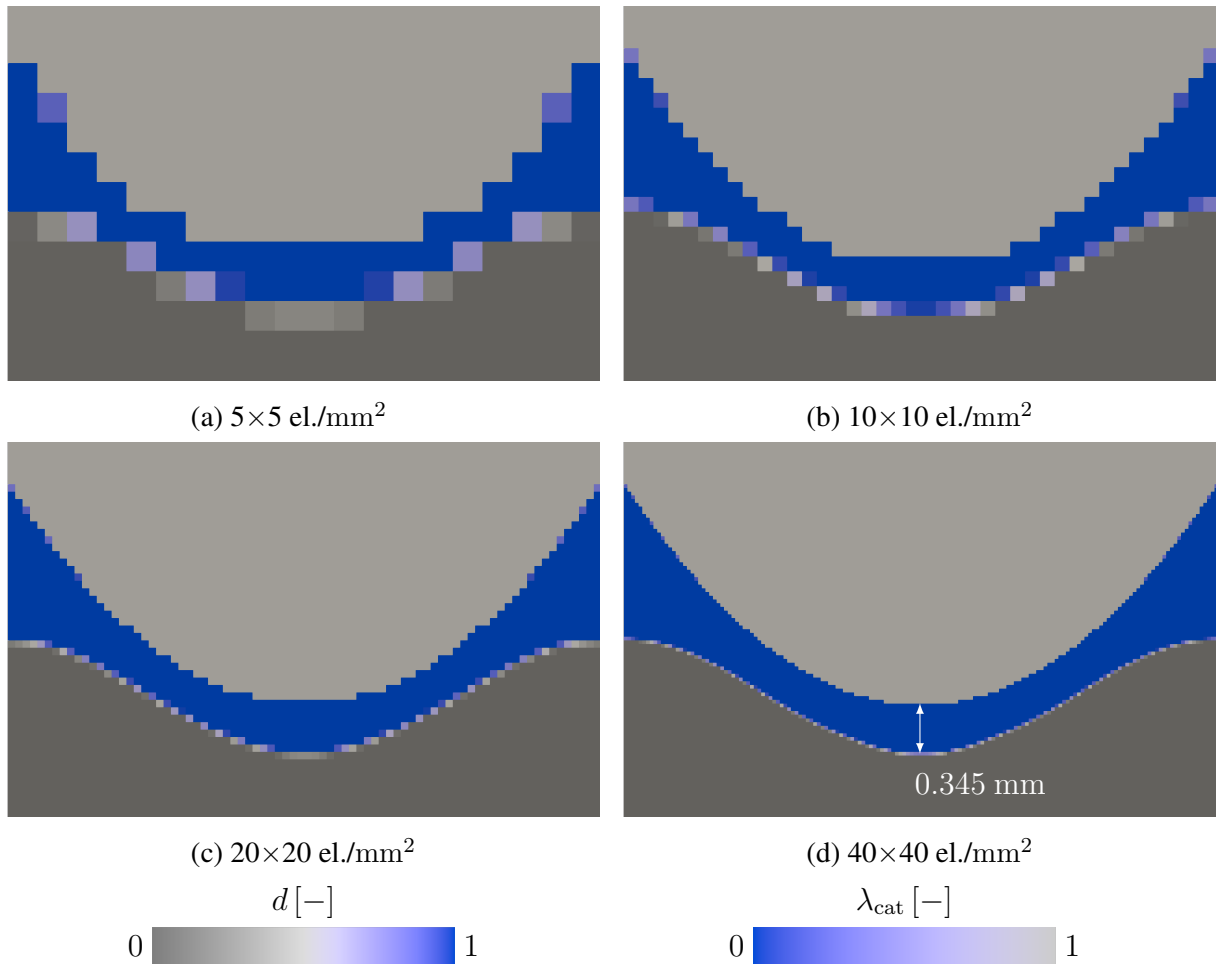


Figure 21: Zoom to the tool tip at the end of the simulation: The dissolution level d and the cathode ratio λ_{cat} show mesh convergence from coarse (Fig. 21a) to fine mesh discretizations (Fig. 21d).

0.35 mm. These results confirm the model’s capabilities to accurately predict the shape of the machined workpiece using coarse meshes.

Furthermore, the runtime of method A and B are compared in this example for different element densities in Fig. 22. For coarse meshes, both methods yield similar runtimes (5×5 el./mm², 10×10 el./mm²). But already for the second finest mesh (20×20 el./mm²), method B is with 21.4 % significantly faster than method A. For the finest mesh (40×40 el./mm²), the savings in computation time are 52.7 %.

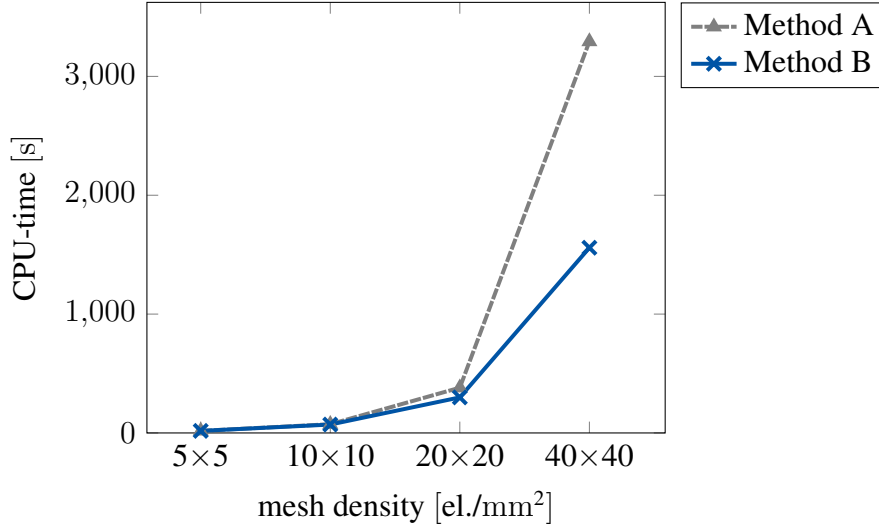


Figure 22: Comparison of the runtime of method A and B. Structured meshes are employed in the simulation with $\Delta t = 0.34483$ s.

Moreover, Fig. 23 shows the evolution of the dissolution level d , the electric potential v and the electric current density j of the problem for two intermediate and the final configuration. Inside the cathode, the electric potential is $v = 0$ V and inside the anode $v \approx 10$ V with a transition zone in the electrolyte. The electric current density initially concentrates in the middle of the specimen leading to a pronounced material removal in this region. With progressing cathode feed, the electric current density’s focus widens mapping a parabolic shape onto the anode.

As discussed in Hardisty and Mileham [1999] and derived in Nilson and Tsuei [1976], a parabolic tool yields a parabolic workpiece. In the current example, a flattening of the workpiece’s surface at the outer edges is observed. The electric field lines are passing perpendicular to the anode’s surface. Here, a zero horizontal flux is prescribed by the Neumann boundary conditions at the outer edge, which, therefore, leads to the flattening of the surface profile in this domain. Fig. 24 shows the machined profile of the specimen with a total length of $10l$. The specimen’s extension releases the zero flux condition at $x = \pm l$ and avoids the pronounced flattening at this position.

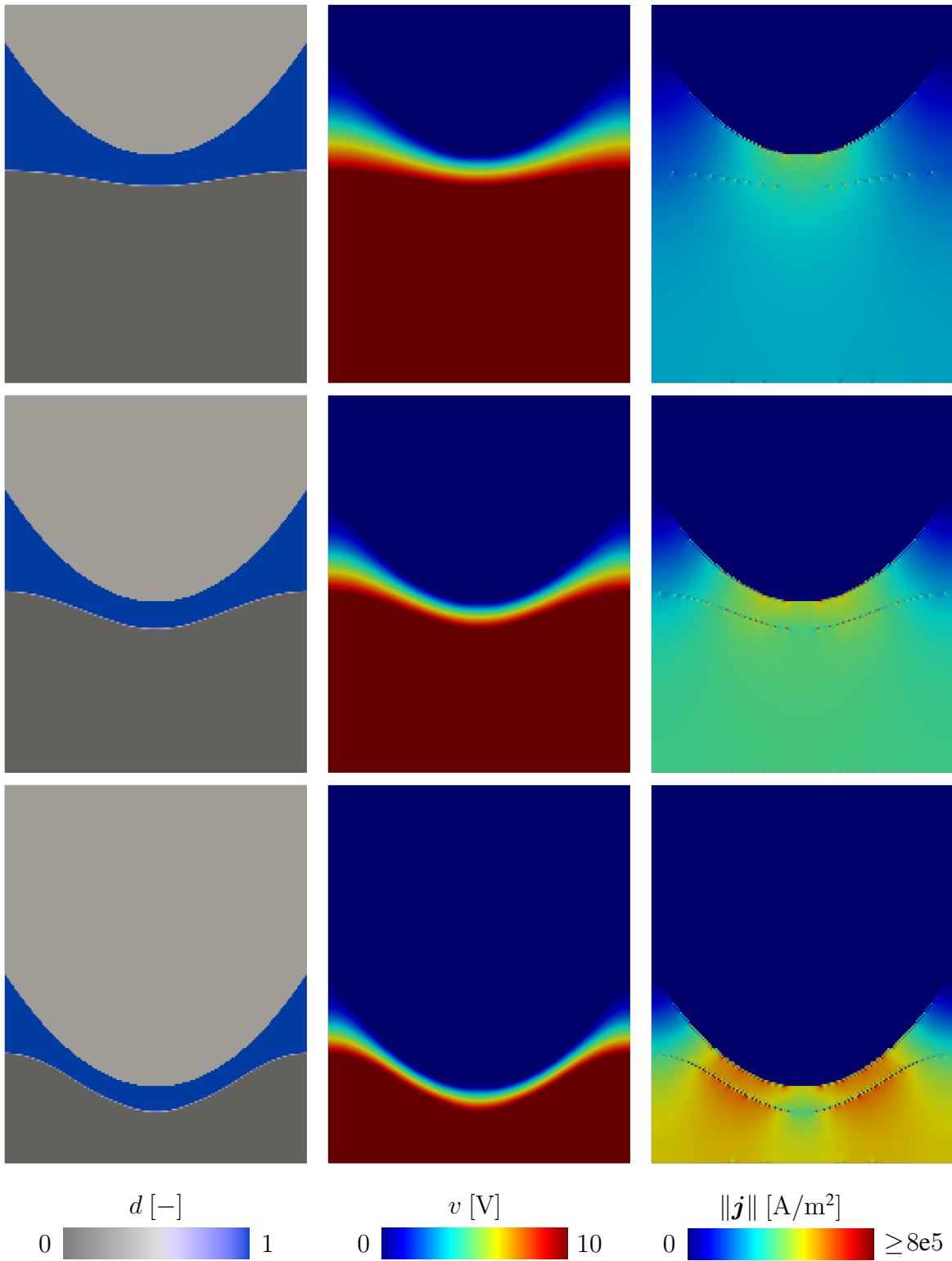


Figure 23: Evolution of the dissolution level d , the electric potential v and the norm of the electric current density $\|\mathbf{j}\|$ for the parabolic cathode at time steps 100, 250 and 500. Due to varying dissolution levels and cathode ratios in adjacent elements, the visualization of the electric current density may yield minor non-uniformities on the surface of the anode and cathode.

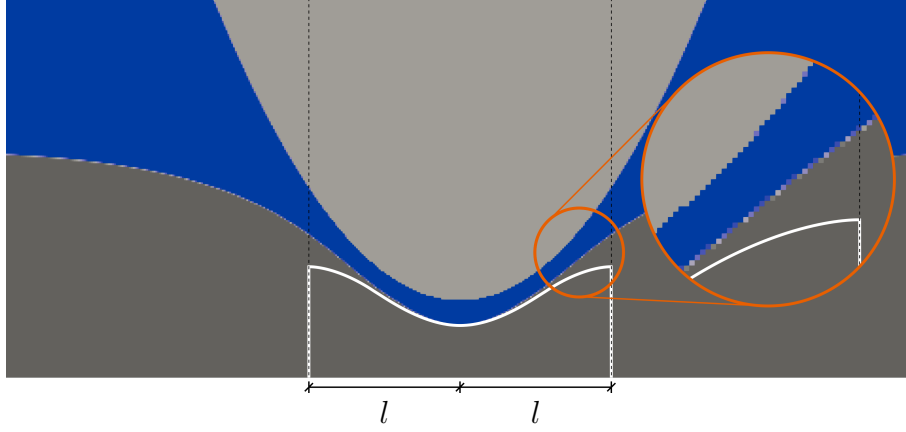


Figure 24: Influence of specimen's length in x -direction on final surface shape. The white line shows the final surface of the specimen with a length of $2l$. The contour plot shows the surface of the specimen with a length of $10l$ in the range of $x \approx \pm 3l$.

6.3 Wire cathode - Sharma et al. [2019]

In the third example, a wire electrochemical machining application is investigated (Fig. 25) and the results are compared with the experiments and simulations of Sharma et al. [2019]. The geometric dimensions read $l_1 = 700 \mu\text{m}$, $l_2 = 50 \mu\text{m}$, $h = 200 \mu\text{m}$, $s = 10 \mu\text{m}$, $r = 15 \mu\text{m}$ with a thickness of $100 \mu\text{m}$. The feed rate is $\dot{x}_{ca} = 4 \mu\text{m/s}$, the potential difference $\Delta v = 6 \text{ V}$ and the electric conductivity $k_E^{\text{EL}} = 1.71 \text{ A}/(\text{V m})$. We set $\nu_{\text{dis}} = 1.09 \times 10^{-11} \text{ m}^3/(\text{A s})$ and $\Delta t = 0.1 \text{ s}$. This example necessitates the use of method B to apply the cathode condition $\tilde{v}_{ca} = 0 \text{ V}$ only locally within the wire.

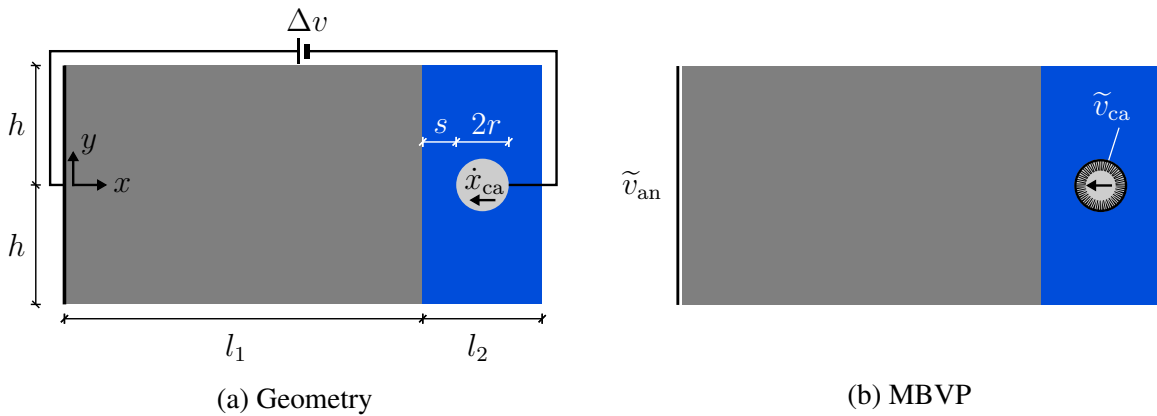


Figure 25: Geometry and moving boundary value problem for a wire tool (cf. Sharma et al. [2019]).

Fig. 26 shows the mesh employed in the simulation which possesses strong refinement in the region of the kerf. Moreover, the orange box in Fig. 26 shows the image section of Fig. 27 where the initial phase of the dissolution process is studied. Here, the dissolution level d and

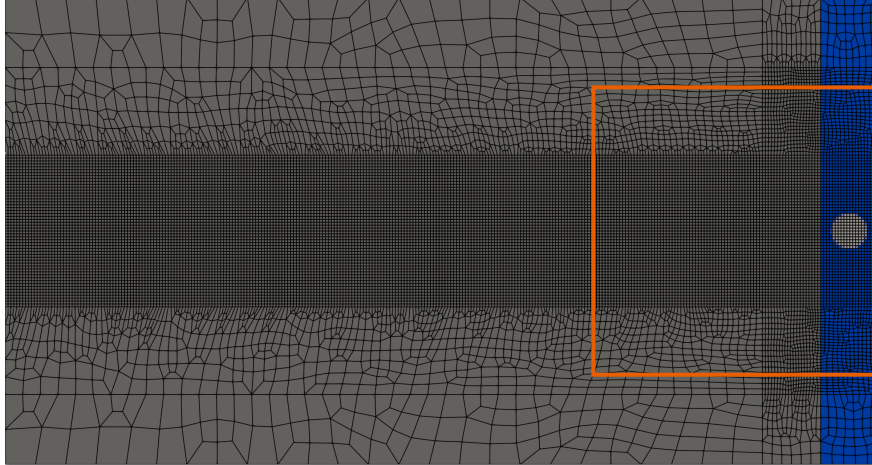


Figure 26: Mesh for wire tool example (19995 elements). The orange box indicates the image section investigated in Fig. 27.

the norm of the electric current density $\|j\|$ are given. Initially, the electric current density exhibits its maximum in horizontal direction, thereby, inducing the highest material removal at this position. Afterwards, the electric current density's scope becomes larger which causes a widening of the kerf. After 25 s, the distribution of the electric current density between wire and work piece remains approximately constant and yields a clean cut.

Fig. 28 shows the final shape of the specimen after a machining time of 150 s. Measuring the kerf width at $x = 400 \mu\text{m}$ yields a width of $118.73 \mu\text{m}$ which is in the range between $110.08 \mu\text{m}$ (experimental kerf width) and $124.27 \mu\text{m}$ (simulated kerf width) of Sharma et al. [2019].

The simulation required 10 h 51 min and, thus, was faster than the simulation with the fine discretization of Sharma et al. [2019] whose code was implemented in MATLAB (R2016a) and required 16 h 03 min. Further speedups are realized by considering an additional moving anode boundary condition. This prescribes $\tilde{v}_{\text{an}} = 6 \text{ V}$ in the region $50 \mu\text{m}$ below the work piece's initial surface and moves horizontally with the cathode's feed rate. Hereby, the computation time is reduced by 59 % to 4 h 28 min and is even faster than the simulation with the coarse discretization of Sharma et al. [2019] with 6 h 19 min.

6.4 Complex cathode - blade machining

Inspired by e.g. Tsuboi and Yamamoto [2009], Klocke et al. [2013] or Zhu et al. [2017], we study in this example a blade machining process with a complex cathode geometry, where two tools move towards an enclosed workpiece.

The material parameters stem from Table 2 and the geometric dimensions (in [mm]) read $l_1 = 4.5$, $s_1 = 1.5$, $l_2 = 10$, $s_2 = 0.35$, $l_3 = 5.65$, $h = 25$ with a thickness of 0.2 (Fig. 29).

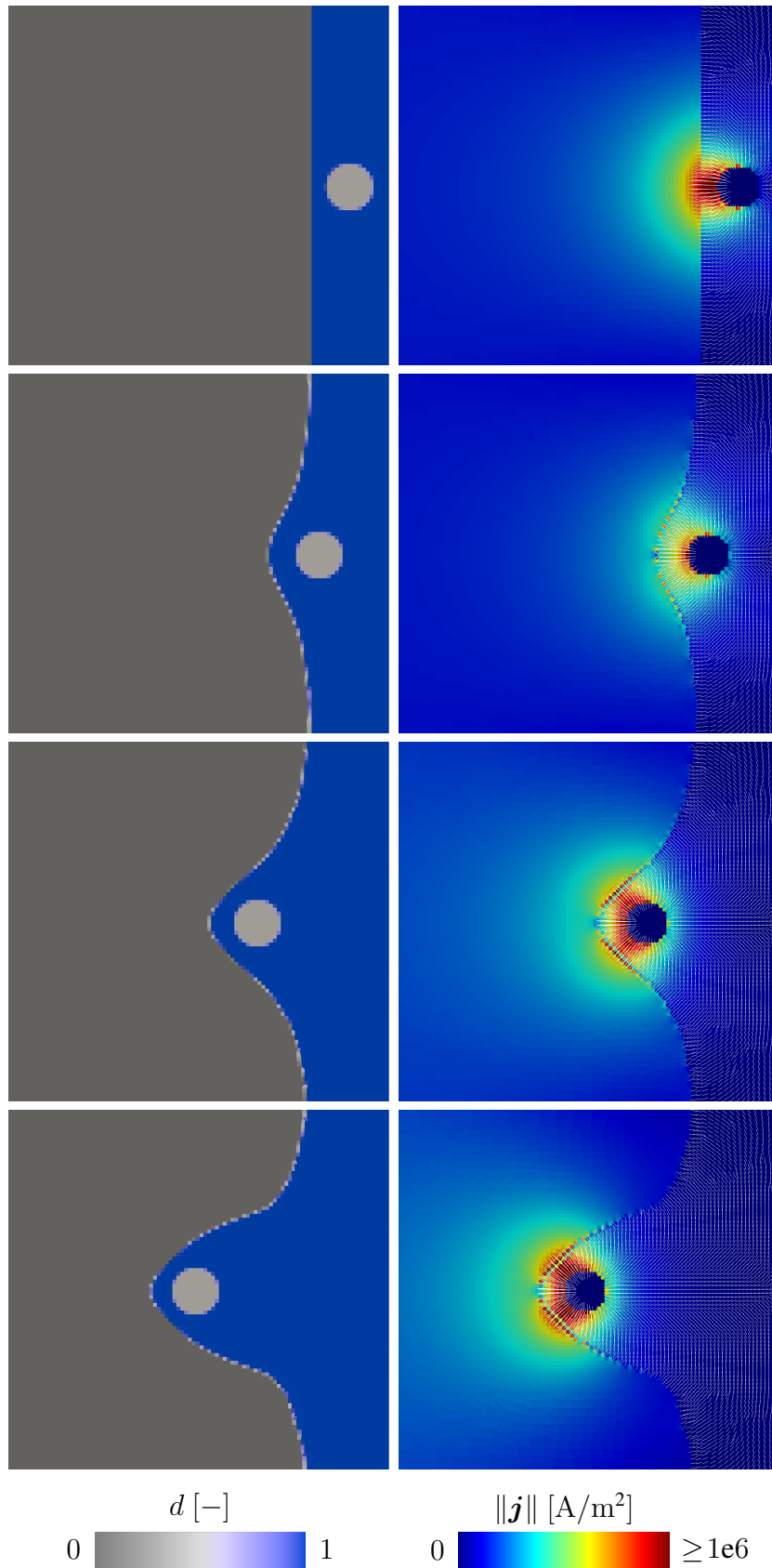


Figure 27: Evolution of the dissolution level d and the norm of the electric current density $\|j\|$, where the white lines show the orientation of the electric field, for the wire tool. Zoom to the right edge of the specimen at time 0 s, 5 s, 15 s and 25 s.

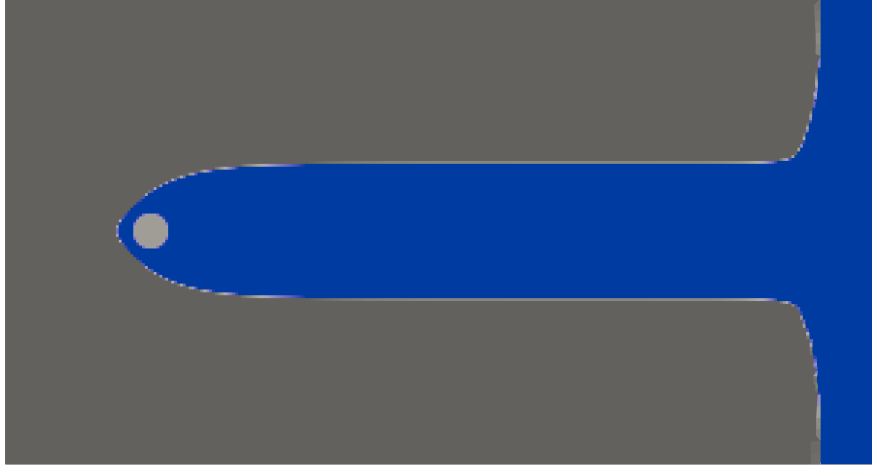


Figure 28: Final shape of the specimen after machining with the wire tool after a machining time of 150 s.

Moreover, the following circles define the cathode's surface with $r_1 = 0.5$ (center: 4 | 0.551), $r_2 = 2$ (center: 4.5 | 3), $r_9 = 0.49$ (center: 16.840 | 0.551). Additionally, the following ellipses complete the surface with $r_3 = 2.8$, $r_4 = 14$ (center: 1.56 | 13.9, rotation: $\alpha_1 = 5.44^\circ$), $r_5 = 11.25$, $r_6 = 4.5$ (center: 16.05 | 13.75, rotation: $\alpha_2 = 11.5^\circ$) and $r_7 = 7.5$, $r_8 = 4.5$ (center: 16.35 | 8.5).

The feed rate is $\dot{x}_{ca} = 0.01$ mm/s and the potential difference $\Delta v = 20$ V with $\tilde{v}_{an} = 20$ V which is prescribed in the region $x \in [11.5, 12]$ and $y \in [3, 20]$. The time increment reads $\Delta t = 2$ s and method B is utilized.

In Fig. 30, the evolution of the dissolution level d and the norm of the electric current density $\|\mathbf{j}\|$ is presented for two intermediate and the final configuration. Due to the initially small working gap width at the top and bottom region of the specimen, we observe a pronounced material removal in these sections. With increasing machining time, the workpiece continuously dissolves also in the middle of the specimen (time 400 s) until finally the mapping of the cathode's shape onto the workpiece is completed (time 580 s).

The simulation required a computation time of 2 h 12 min and, thus, confirms the method's ability to model complex dissolution processes with good efficiency.

7 Conclusion

In this paper, a novel methodology to model the cathode feed in the moving boundary value problem of electrochemical machining was presented. Two approaches are investigated to describe the cathode. In method A, which is characterized by a simple and robust implementation,

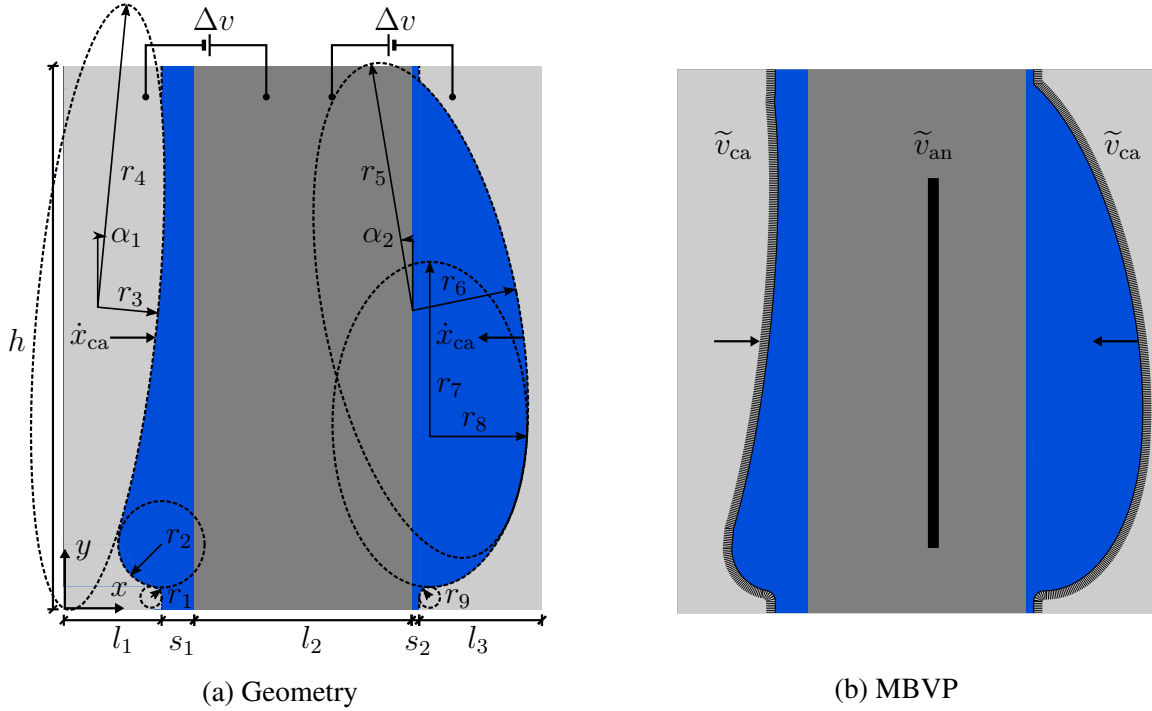


Figure 29: Geometry and moving boundary value problem with complex cathode shape.

the electric conductivities of cathode elements are modified. In method B, Dirichlet boundary conditions are applied on all nodes within the cathode and, hence, facilitate considerable speedups. Elements on the cathode's surface are described by effective material parameters. The model's accuracy is confirmed by analytical as well as experimental and numerical reference solutions from the literature. Moreover, low runtimes allow for the efficient investigation of complex shapes.

The presented model formulation is focused on the efficient description of the cathode feed in ECM simulations. Currently, it considers only certain aspects of the multiphysical process. Thus, further work includes the modeling of multiphase materials (cf. Kozak and Zyburas-Skrabalak [2016], Harst [2019]) and the formation of oxide layers (e.g. Zander et al. [2021]) to incorporate the polarization voltage. Moreover, a formulation of the dissolution model in the gradient enhanced framework, which was introduced by e.g. Dimitrijevic and Hackl [2008] and Forest [2009, 2016] and applied in e.g. Brepols et al. [2017, 2020] and Fassin et al. [2019a,b], can be investigated. Further, the consideration of mass transfer, hydrogen generation and fluid mechanical effects following Deconinck et al. [2012a,b, 2013] would yield a valuable model extension.

Finally, a transfer of the modeling technique to laserchemical machining (LCM, e.g. Schupp et al. [2021]) is aspired, which requires to adapt the evolution equation of the dissolution level from an electrically to a thermally based formulation (Klocke et al. [2016]).

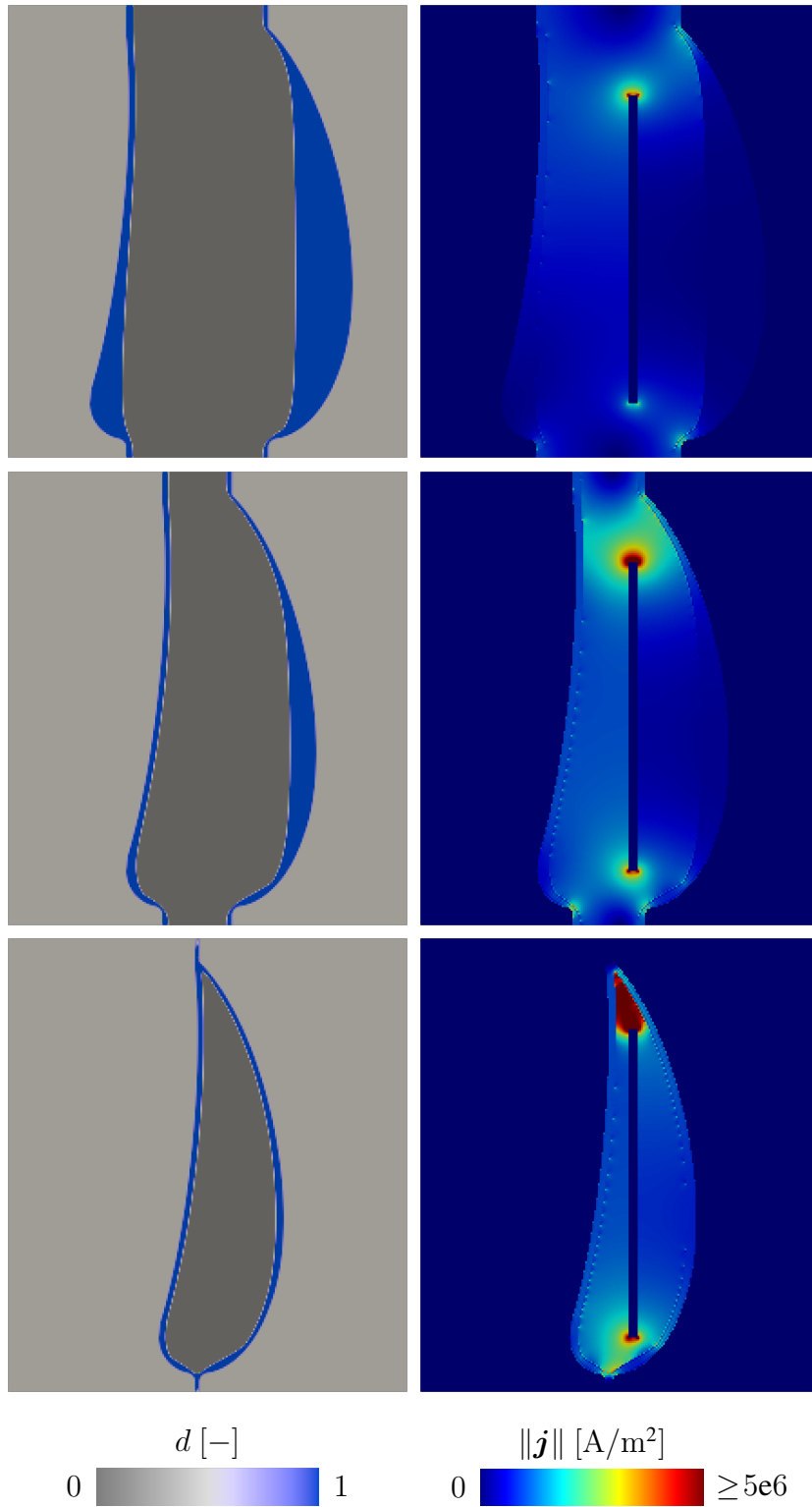


Figure 30: Evolution of the dissolution level d and the norm of the electric current density $\|j\|$ for a complex cathode at times 200 s, 400 s and 580 s .

Acknowledgements

Funding granted by the German Research Foundation (DFG) for projects number 453715964, 223500200 (M05) and 417002380 (A01) is gratefully acknowledged.

References

- Alkire, R., Bergh, T. and Sani, R. L. [1978], ‘Predicting electrode shape change with use of finite element methods’, *Journal of The Electrochemical Society* **125**(12), 1981–1988.
- Antonova, E. E. and Looman, D. C. [2005], ‘Finite elements for thermoelectric device analysis in ansys’, *IEEE. ICT 2005. 24th International Conference on Thermoelectrics* **2005**, 215–218.
- Barfusz, O., van der Velden, T., Brepols, T., Holthusen, H. and Reese, S. [2021], ‘A reduced integration-based solid-shell finite element formulation for gradient-extended damage’, *Computer Methods in Applied Mechanics and Engineering* **382**, 113884.
- Barfusz, O., van der Velden, T., Brepols, T. and Reese, S. [2022], ‘Gradient-extended damage analysis with reduced integration-based solid-shells at large deformations’, *Computer Methods in Applied Mechanics and Engineering* **389**, 114317.
- Brepols, T., Wulfinghoff, S. and Reese, S. [2017], ‘Gradient-extended two-surface damage-plasticity: Micromorphic formulation and numerical aspects’, *International Journal of Plasticity* **97**, 64 – 106.
- Brepols, T., Wulfinghoff, S. and Reese, S. [2020], ‘A gradient-extended two-surface damage-plasticity model for large deformations’, *International Journal of Plasticity* **129**, 102635.
- Brookes, D. [1984], *Computer-Aided Shape Prediction of Electro-chemically Machined Work Using the Method of Finite Elements*, The University of Manchester (PhD Thesis).
- Christiansen, S. and Rasmussen, H. [1976], ‘Numerical solutions for two-dimensional annular electrochemical machining problems’, *Journal of the Institute of Mathematics and its Applications* **18**, 295–307.
- DeBarr, A. E. and Oliver, D. A. [1968], *Electrochemical Machining*, Macdonald & Co. Ltd, London.
- Deconinck, D., Hoogsteen, W. and Deconinck, J. [2013], ‘A temperature dependent multi-ion model for time accurate numerical simulation of the electrochemical machining process. part iii: Experimental validation’, *Electrochimica Acta* **103**, 161 – 173.

- Deconinck, D., Van Damme, S., Albu, C., Hotoiu, L. and Deconinck, J. [2011], ‘Study of the effects of heat removal on the copying accuracy of the electrochemical machining process’, *Electrochimica Acta* **56**(16), 5642–5649.
- Deconinck, D., Van Damme, S. and Deconinck, J. [2012a], ‘A temperature dependent multi-ion model for time accurate numerical simulation of the electrochemical machining process. part i: Theoretical basis’, *Electrochimica Acta* **60**, 321 – 328.
- Deconinck, D., Van Damme, S. and Deconinck, J. [2012b], ‘A temperature dependent multi-ion model for time accurate numerical simulation of the electrochemical machining process. part ii: Numerical simulation’, *Electrochimica Acta* **69**, 120 – 127.
- Deconinck, J., Maggetto, G. and Vereecken, J. [1985], ‘Calculation of current distribution and electrode shape change by the boundary element method’, *Journal of The Electrochemical Society* **132**(12), 2960–2965.
- Dimitrijevic, B. and Hackl, K. [2008], ‘A method for gradient enhancement of continuum damage models’, *Technische Mechanik-European Journal of Engineering Mechanics* **28**(1), 43–52.
- Fasano, A. and Primicerio, M. [1983], *Free boundary problems: theory and applications*, Vol. 2, Pitman Advanced Publishing Program.
- Fassin, M., Eggersmann, R., Wulfinghoff, S. and Reese, S. [2019a], ‘Efficient algorithmic incorporation of tension compression asymmetry into an anisotropic damage model’, *Computer Methods in Applied Mechanics and Engineering* **354**, 932–962.
- Fassin, M., Eggersmann, R., Wulfinghoff, S. and Reese, S. [2019b], ‘Gradient-extended anisotropic brittle damage modeling using a second order damage tensor – theory, implementation and numerical examples’, *International Journal of Solids and Structures* **167**, 93–126.
- Forest, S. [2009], ‘Micromorphic approach for gradient elasticity, viscoplasticity, and damage’, *Journal of Engineering Mechanics* **135**(3), 117–131.
- Forest, S. [2016], ‘Nonlinear regularization operators as derived from the micromorphic approach to gradient elasticity, viscoplasticity and damage’, *Proceedings of the Royal Society A: Mathematical, Physical and Engineering Sciences* **472**(2188), 20150755.
- Hardisty, H. and Mileham, A. [1999], ‘Finite element computer investigation of the electrochemical machining process for a parabolically shaped moving tool eroding an arbitrarily shaped workpiece’, *Proceedings of the Institution of Mechanical Engineers, Part B: Journal of Engineering Manufacture* **213**(8), 787–798.
- Hardisty, H., Mileham, A. R., Shirvarni, H. and Bramley, A. N. [1993], ‘A finite element simulation of the electrochemical machining process’, *CIRP annals* **42**(1), 201–204.

- Harst, S. [2019], *Entwicklung einer Prozesssignatur für die elektrochemische Metallbearbeitung*, Apprimus Wissenschaftsverlag.
- Hinduja, S. and Kunieda, M. [2013], ‘Modelling of ecm and edm processes’, *CIRP Annals* **62**(2), 775 – 797.
- Hofmann, T., Westhoff, D., Feinauer, J., Andrä, H., Zausch, J., Schmidt, V. and Müller, R. [2020], ‘Electro-chemo-mechanical simulation for lithium ion batteries across the scales’, *International Journal of Solids and Structures* **184**, 24–39.
- Holthusen, H., Brepols, T., Reese, S. and Simon, J.-W. [2020], ‘An anisotropic constitutive model for fiber-reinforced materials including gradient-extended damage and plasticity at finite strains’, *Theoretical and Applied Fracture Mechanics* **108**, 102642.
- Hughes, T. J. R. [1987], *The Finite Element Method: Linear Static and Dynamic Finite Element Analysis*, Prentice Hall, Englewood Cliffs, NJ.
- Jackson, J. D. [1962], *Classical Electrodynamics*, John Wiley & Sons Ltd.
- Jain, V. and Pándey, P. [1980], ‘Finite element approach to the two dimensional analysis of electrochemical machining’, *Precision Engineering* **2**(1), 23–28.
- Joe, B. [1991], ‘Geompack—a software package for the generation of meshes using geometric algorithms’, *Advances in Engineering Software and Workstations* **13**(5-6), 325–331.
- Juhre, D. and Reese, S. [2010], ‘A reduced integration finite element technology based on a thermomechanically consistent stabilisation for 3d problems’, *Computer Methods in Applied Mechanics and Engineering* **199**(29), 2050–2058.
- Kachanov, L. M. [1958], ‘Time of the rupture process under creep conditions’, *TVZ Akad Nauk S.S.R. Otd Tech. Nauk* **8**, 26–31.
- Klocke, F., Heidemanns, L., Zeis, M. and Klink, A. [2018], ‘A novel modeling approach for the simulation of precise electrochemical machining (pecm) with pulsed current and oscillating cathode’, *Procedia CIRP* **68**, 499–504.
- Klocke, F., Klink, A., Veselovac, D., Aspinwall, D. K., Soo, S. L., Schmidt, M., Schilp, J., Levy, G. and Kruth, J.-P. [2014], ‘Turbomachinery component manufacture by application of electrochemical, electro-physical and photonic processes’, *CIRP Annals* **63**(2), 703–726.
- Klocke, F. and König, W. [2007], *Fertigungsverfahren 3 Abtragen, Generieren und Lasermaterialbearbeitung*, Springer.
- Klocke, F., Vollertsen, F., Harst, S., Eckert, S., Zeis, M., Klink, A. and Mehrafsun, S. [2016], ‘Comparison of material modifications occurring in laserchemical and electrochemical machining’, *Proceedings INSECT* **12**, 57–63.

- Klocke, F., Zeis, M., Harst, S., Klink, A., Veselovac, D. and Baumgärtner, M. [2013], ‘Modeling and simulation of the electrochemical machining (ecm) material removal process for the manufacture of aero engine components’, *Procedia CIRP* **8**, 265–270.
- Koenig, W. and Huembs, H. [1977], ‘Mathematical model for the calculation of the contour of the anode in electrochemical machining’, *Annals of the CIRP* **25**, 83–87.
- Kozak, J. [1998], ‘Mathematical models for computer simulation of electrochemical machining processes’, *Journal of Materials Processing Technology* **76**, 170–175.
- Kozak, J. and Zybura-Skrabalak, M. [2016], ‘Some problems of surface roughness in electrochemical machining (ecm)’, *Procedia CIRP* **42**, 101 – 106.
- Liu, Q., Liu, M., Li, H. and Lam, K. [2020], ‘Multiphysics modeling of responsive deformation of dual magnetic-ph-sensitive hydrogel’, *International Journal of Solids and Structures* **190**, 76–92.
- McGeough, J. A. [1974], *Principles of electrochemical machining*, Chapman & Hall.
- Narayanan, O., Hinduja, S. and Noble, C. [1986], ‘The prediction of workpiece shape during electrochemical machining by the boundary element method’, *International Journal of Machine Tool Design and Research* **26**(3), 323–338.
- Nilson, R. H. and Tsuei, Y. G. [1976], ‘Free Boundary Problem for the Laplace Equation With Application to ECM Tool Design’, *Journal of Applied Mechanics* **43**(1), 54–58.
- Pérez-Aparicio, J. L., Taylor, R. L. and Gavela, D. [2007], ‘Finite element analysis of nonlinear fully coupled thermoelectric materials’, *Computational Mechanics* **40**(1), 35–45.
- Rajurkar, K., Sundaram, M. and Malshe, A. [2013], ‘Review of electrochemical and electrodischarge machining’, *Procedia CIRP* **6**, 13–26.
- Reese, S., Brepols, T., Fassin, M., Poggenpohl, L. and Wulfinghoff, S. [2021], ‘Using structural tensors for inelastic material modeling in the finite strain regime – a novel approach to anisotropic damage’, *Journal of the Mechanics and Physics of Solids* **146**, 104174.
- Reese, S., Svendsen, B., Stiemer, M., Unger, J., Schwarze, M. and Blum, H. [2005], ‘On a new finite element technology for electromagnetic metal forming processes’, *Archive of Applied Mechanics* **74**(11), 834–845.
- Schupp, A., Pütz, R. D., Beyss, O., Beste, L.-H., Radel, T. and Zander, D. [2021], ‘Change of oxidation mechanisms by laser chemical machined rim zone modifications of 42crmo4 steel’, *Materials* **14**(14), 3910.

- Sharma, V., Srivastava, I., Jain, V. and Ramkumar, J. [2019], ‘Modelling of wire electrochemical micromachining (wire-ecmm) process for anode shape prediction using finite element method’, *Electrochimica Acta* **312**, 329–341.
- Taylor, R. L. and Govindjee, S. [2020], ‘FEAP - - a finite element analysis program’, *University of California, Berkeley* .
URL: http://projects.ce.berkeley.edu/feap/manual_86.pdf
- Tipton, H. [1964], ‘The dynamics of electrochemical machining’, *Proc. 5th Int. MTDR Conf, University of Birmingham Birmingham* pp. 509–522.
- Tsuboi, R. and Yamamoto, M. [2009], ‘Modeling and applications of electrochemical machining process’, *ASME International Mechanical Engineering Congress and Exposition* **4**, 377–384.
- van der Velden, T., Rommes, B., Klink, A., Reese, S. and Waimann, J. [2021], ‘A novel approach for the efficient modeling of material dissolution in electrochemical machining’, *International Journal of Solids and Structures* **229**, 111106.
- Wu, T. and Li, H. [2018], ‘Phase-field model for liquid–solid phase transition of physical hydrogel in an ionized environment subject to electro–chemo–thermo–mechanical coupled field’, *International Journal of Solids and Structures* **138**, 134–143.
- Wuilbaut, T. A. [2008], *Algorithmic developments for a multiphysics framework*, (Unpublished doctoral dissertation). Université libre de Bruxelles, Faculté des sciences appliquées – Mécanique, Bruxelles.
- Zander, D., Schupp, A., Beyss, O., Rommes, B. and Klink, A. [2021], ‘Oxide formation during transpassive material removal of martensitic 42crmo4 steel by electrochemical machining’, *Materials* **14**(2), 402.
- Zhu, D., Zhao, J., Zhang, R. and Yu, L. [2017], ‘Electrochemical machining of blades with cross-structural cathodes at leading/trailing edges’, *The International Journal of Advanced Manufacturing Technology* **93**(9), 3221–3228.
- Zienkiewicz, O. C., Taylor, R. L. and Zhu, J. Z. [2005], *The finite element method: its basis and fundamentals*, Elsevier.